Journal of Rock Mechanics and Geotechnical Engineering 6 (2014) 77–98

Contents lists available at ScienceDirect

Journal of Rock Mechanics and Geotechnical Engineering

journal homepage: www.rockgeotech.org

Thermo-hydro-mechanical-air coupling finite element method and its application to multi-phase problems

Feng Zhang [a,*], Yonglin Xiong [a], Sheng Zhang [b], Bin Ye [c]

[a] Department of Civil Engineering, Nagoya Institute of Technology, Showa-ku, Gokiso-cho, Nagoya, 466-8555, Japan
[b] Department of Civil Engineering, Central South University, Changsha, 410075, China
[c] Department of Civil Engineering, Tongji University, Shanghai, 200092, China

ARTICLE INFO

Article history:
Received 2 January 2014
Received in revised form
15 January 2014
Accepted 28 January 2014
Available online 5 February 2014

Keywords:
Multi-phase
Thermo-hydro-mechanical-air (THMA)
Finite element method (FEM)
Finite deformation
Constitutive model
Unified field equations

ABSTRACT

In this paper, a finite element method (FEM)-based multi-phase problem based on a newly proposed thermal elastoplastic constitutive model for saturated/unsaturated geomaterial is discussed. A program of FEM named as SOFT, adopting unified field equations for thermo-hydro-mechanical-air (THMA) behavior of geomaterial and using finite element-finite difference (FE-FD) scheme for soil–water–air three-phase coupling problem, is used in the numerical simulation. As an application of the newly proposed numerical method, two engineering problems, one for slope failure in unsaturated model ground and another for in situ heating test related to deep geological repository of high-level radioactive waste (HLRW), are simulated. The model tests on slope failure in unsaturated Shirasu ground, carried out by Kitamura et al. (2007), is simulated in the framework of soil–water–air three-phase coupling under the condition of constant temperature. While the in situ heating test reported by Munoz (2006) is simulated in the same framework under the conditions of variable temperature but constant air pressure.

1. Introduction

Multi-phase issue has attracted more attention recently because of its wide involvement in geotechnical engineering problems, not only in instant failure problem like slope failure, but also in long-term stability problem like deep geological repository of high-level radioactive waste (HLRW). Numerous researches, both in laboratory/field tests and numerical simulation/prediction, have been conducted in this field ceaselessly. Yet it is still far away from the state with which we can satisfy. The key problem is that, in most cases, people have to simplify a real geotechnical problem with some assumptions and to pick up one or several factors they think the most important and take them as their concerns while other factors are neglected. For instance, constitutive model is always divided into two parts, one for saturated material and another for unsaturated. Thermal and viscoplastic effects are the other questions needed to be addressed. What we want to emphasize here is that, the physical states, such as the saturation (S_r) or the temperature (T) are only the states of a geomaterial, you cannot say that the geomaterial is a different material when the states are different. Unfortunately, in most cases, a constitutive model usually merely considers the geomaterial in a specific state; in other words, it can describe the mechanical behavior of the geomaterial in the specific state but cannot fit anymore at other states.

As is known, geomaterial is different from some other engineering materials such as steel and concrete in that it consists of more than one phase. Geomaterials are usually made of soil grain, water and air. When the voids are fully occupied with water, soil is called as saturated soil, otherwise unsaturated soil. Followed by the pioneering work (Alonso et al., 1990), in which Barcelona Basic Model (BBM), a fundamental model for unsaturated soil, was proposed using the concept of loading-collapse (LC) and suction increase (SI), a number of elastoplastic constitutive models have been developed to describe the behavior of unsaturated soil. Some of these models were proposed in the framework of net stress and suction such as Cui and Delage (1996), Chiu and Ng (2003), and Sheng et al. (2008), whereas others are in the framework of Bishop-type effective stress and suction such as Kohgo et al. (1993), Loret and Khalili (2002), and Sun et al. (2007). More recently, some constitutive models using the effective stress and the degree of saturation as independent state variables have been proposed, such as Ohno et al. (2007), Zhang and Ikariya (2011), and Zhou et al.

* Corresponding author. Tel.: +81 0527357923.
E-mail addresses: cho.ho@nitech.ac.jp, zhangkeyinjp@gmail.com (F. Zhang).
Peer review under responsibility of Institute of Rock and Soil Mechanics, Chinese Academy of Sciences.

Production and hosting by Elsevier

1674-7755
http://dx.doi.org/10.1016/j.jrmge.2014.01.010

(2012a,b). As pointed out by Zhang and Ikariya (2011), using the effective stress and the degree of saturation in modeling unsaturated soil is much easier and smoother to describe the behavior of soil from unsaturated state to saturated state than that using the net stress or effective stress and the suction as the independent state variables.

On the other hand, researches related to the thermal effect on geomaterials have also been done extensively due to the huge demand for assessing the safety of deep geological repository of HLRW. Until now, a number of experimental studies have been conducted to investigate the thermal effects on mechanical behaviors of the saturated geomaterials, e.g. Campanella and Mitchell (1968), Baldi et al. (1988, 1991), Cekerevac and Laloui (2004), Okada (2005), and Nishimura (2013).

At the same time, many constitutive models for saturated geomaterials considering thermal effects have been proposed, e.g. the works by Cui et al. (2000, 2009), Laloui (2001), Zhang and Zhang (2009), and Zhang et al. (2012). In comparison with the saturated geomaterials, researches related to the thermal effects on unsaturated soils were rarely reported because of the difficulty for independent measurement and control of pore air pressure (PAP), pore water pressure (PWP), mechanical loading and temperature at the same time. Yet the researches on the modeling of unsaturated geomaterials under non-isothermal condition can be found in the literature. Francois and Laloui (2008) proposed a unified thermo-mechanical model for unsaturated soils, in which the temperature and suction effects are studied within the framework of elastoplastic theorem. Dumont et al. (2011) proposed a thermo-hydro-mechanical (THM) model for unsaturated soils based on the extension of effective stress concept to unsaturated soils using a capillary stress. Uchaipichat and Khalili (2009) conducted a comprehensive non-isothermal test on compacted samples of silt with triaxial loading device.

Meanwhile, the THM behaviors of artificial and natural barriers in the deep geological repository of HLRW have also been investigated intensively, both in experiment and numerical simulation. A lot of field heating experiments have been reported in the last decades, such as the works by Gens et al. (2007, 2009), Jia et al. (2007), Akesson et al. (2009), Gens (2010), and Sawada et al. (2009). In reality, however, the heating period caused by the HLRW will last for hundreds thousands years or even longer for some radioactive substances. Therefore, sometime it is impossible to reproduce the whole process in the field tests. Numerical simulation would be a potential effective method to describe and predict the THM behaviors on the condition that the numerical method is able to fit the results of field experiments, at least in a limited period of time. For this reason, the laboratory tests on the THM behaviors of geomaterials at element level will play an important role in improving the accuracy of the numerical analyses. Many laboratory element tests of geomaterials have been conducted in order to investigate the basic thermo-mechanical behavior. It is overwhelmingly reported that the strength of geomaterial will decrease when its temperature increases, e.g. the works performed by Okada (2005, 2006) and Nishimura (2013). Volumetric change of geomaterials induced by heating was also conducted by Towhata et al. (1993), Laloui and Cekerevac (2003), and Cekerevac and Laloui (2004).

As to the numerical methods in multi-phase problems, many works can be found in the literature, e.g. the work related to soil–water two-phase coupling problem by Oka et al. (1994) and the works related to the soil–water–air three-phase coupling problem by Li et al. (2004), Borja (2005), Uzuoka et al. (2007, 2008, 2009), Uzuoka (2010), and Oka et al. (2010). In the works related to finite element-finite difference (FE-FD) scheme (Oka et al., 1994) for soil–water coupling problem, finite element method (FEM) is used for the spatial discretization of the equilibrium equation and the energy conservation equation, while the backward finite difference scheme proposed by Akai and Tamura (1978) is used for the spatial discretization of the continuity equation. In the works related to THM coupling problem by Oka et al. (2010), the THM coupling relations are based on the work conducted by Nguyen (1995).

The aim of this paper is to establish a unified numerical method to treat the multi-phase problem related to the thermo-hydro-mechanical-air (THMA) behavior of geomaterials, based on a newly proposed thermo-elastoplastic constitutive model for unsaturated/saturated soil (Xiong, 2013). A FEM program, named as SOFT that adopts unified field equations in finite deformation scheme and uses FE-FD scheme for discretizing thermo-soil–water–air coupling problem, is employed in the numerical simulation. As an application of the newly proposed numerical method, two engineering problems, one for slope failure in unsaturated model Shirasu ground (Kitamura et al., 2007) and another for in situ heating test related to deep geological repository of HLRW (Munoz, 2006), are simulated to verify the availability of the proposed numerical method.

2. Thermo-hydro-mechanical-air coupling finite deformation algorithm of field equations

In deriving the unified field equations for the THMA coupling problem in finite deformation algorithm for geomaterials, the following assumptions are adopted:

(1) The distribution of porosity, n, in space and time is very small compared with other variables.
(2) The distribution of degree of saturation, S_r, in space is very small compared with other variables.
(3) The relative acceleration of the fluid (water and air) phase to the solid phase is much smaller than that of the solid phase.
(4) Soil grain is incompressible.

In the following context, the superscripts “s”, “w” and “a” represent the soil, the liquid and the air phases, respectively.

2.1. Equilibrium equation

First of all, definition of appearance density is introduced. The appearance densities of the solid phase $\overline{\rho}^s$, the liquid phase $\overline{\rho}^w$ and the air phase $\overline{\rho}^a$ are defined as

$$\left.\begin{aligned}\overline{\rho}^s &= (1-n)\rho^s\\ \overline{\rho}^w &= nS_r\rho^w\\ \overline{\rho}^a &= n(1-S_r)\rho^a\end{aligned}\right\} \tag{1}$$

where ρ^s, ρ^w and ρ^a are the densities of soil, liquid and air, respectively; n is the porosity of the soil; and S_r is the degree of saturation.

With the use of appearance densities, the density of the three-phase mixture can be expressed as

$$\rho = \overline{\rho}^s + \overline{\rho}^w + \overline{\rho}^a = (1-n)\rho^s + n[S_r\rho^w + (1-S_r)\rho^a] \tag{2}$$

Considering the mean pore pressure p^F, the relationship between total stress tensor $\boldsymbol{T}$ and effective stress tensor $\boldsymbol{T}'$ are as follows:

$$\left.\begin{aligned}\boldsymbol{T} &= \boldsymbol{T}' + p^F\boldsymbol{I}\\ \dot{\boldsymbol{T}} &= \dot{\boldsymbol{T}}' + \dot{p}^F\boldsymbol{I}\\ p^F &= S_r p^w + (1-S_r)p^a\end{aligned}\right\} \tag{3}$$

where $\boldsymbol{I}$ is the identity tensor.

The total stress tensor and the stress tensors (soil, water and air) acting on each phase have the following form:

$$\boldsymbol{T} = \boldsymbol{T}^{\mathrm{s}} + \boldsymbol{T}^{\mathrm{w}} + \boldsymbol{T}^{\mathrm{a}} \tag{4}$$

$$\left.\begin{aligned} \boldsymbol{T}^{\mathrm{s}} &= \boldsymbol{T}' + (1-n)p^{\mathrm{F}}\boldsymbol{I} \\ \boldsymbol{T}^{\mathrm{w}} &= nS_{\mathrm{r}}p^{\mathrm{w}}\boldsymbol{I} \\ \boldsymbol{T}^{\mathrm{a}} &= n(1-S_{\mathrm{r}})p^{\mathrm{a}}\boldsymbol{I} \end{aligned}\right\} \tag{5}$$

Some gradient tensors used in the derivation are defined as follows:

$$\left.\begin{aligned} \boldsymbol{L} &= \left(\frac{\partial v_i}{\partial x_j}\right)\boldsymbol{e}_i \otimes \boldsymbol{e}_j \\ \boldsymbol{D} &= \frac{1}{2}\left(\frac{\partial v_i}{\partial x_j} + \frac{\partial v_j}{\partial x_i}\right)\boldsymbol{e}_i \otimes \boldsymbol{e}_j \\ \boldsymbol{W} &= \frac{1}{2}\left(\frac{\partial v_i}{\partial x_j} - \frac{\partial v_j}{\partial x_i}\right)\boldsymbol{e}_i \otimes \boldsymbol{e}_j \end{aligned}\right\} \tag{6}$$

where $\boldsymbol{L}$ is the velocity gradient tensor, $\boldsymbol{D}$ is the strain rate tensor or stretching tensor, $\boldsymbol{W}$ is the rotation rate tensor, v_i is the velocity vector, v_j is strain rate vector, and $\boldsymbol{e}_i \otimes \boldsymbol{e}_j$ is the base of tensor. There is a relationship of $\boldsymbol{L} = \boldsymbol{D} + \boldsymbol{W}$. The definitions of the above three tensors can be applied to three phases.

The constitutive equation of each phase can be defined as

$$\overset{\nabla}{\boldsymbol{T}} = \boldsymbol{C} : \boldsymbol{D}^{\mathrm{s}} \text{ or } \mathring{\boldsymbol{T}} = \boldsymbol{C} : \boldsymbol{D}^{\mathrm{s}} \tag{7}$$

$$\left.\begin{aligned} \dot{p}^{\mathrm{w}} &= K^{\mathrm{w}}\mathrm{tr}(\boldsymbol{D}^{\mathrm{w}}) \\ \dot{p}^{\mathrm{a}} &= K^{\mathrm{a}}\mathrm{tr}(\boldsymbol{D}^{\mathrm{a}}) \end{aligned}\right\} \tag{8}$$

where $\overset{\nabla}{\boldsymbol{T}}$ is the Jaumann stress rate tensor or $\mathring{\boldsymbol{T}}$ the Green–Naghdi stress rate tensor; $\boldsymbol{C}$ is the stiffness tensor, which is a fourth-order tensor; K^{w} and K^{a} are the volumetric stiffness of liquid and air phases, respectively.

As to the relative velocities $\dot{\boldsymbol{w}}^{\mathrm{w}}$ between solid and liquid phases, and $\dot{\boldsymbol{w}}^{\mathrm{a}}$ between solid and air phases, Darcy's law is assumed to be still valid, thus we have

$$\begin{aligned} \dot{\boldsymbol{w}}^{\mathrm{w}} &= -k^{\mathrm{w}}\frac{\partial h^{\mathrm{w}}}{\partial x} = -k^{\mathrm{w}}\frac{\partial\left(h_{\mathrm{d}}^{\mathrm{w}} + h_{\mathrm{ini}}^{\mathrm{w}}\right)}{\partial x} = -k^{\mathrm{w}}\frac{\partial}{\partial x}\left(\frac{p_{\mathrm{d}}^{\mathrm{w}}}{\gamma^{\mathrm{w}}} + h_{\mathrm{ini}}^{\mathrm{w}}\right) \\ &= -\frac{k^{\mathrm{w}}}{\gamma^{\mathrm{w}}}\frac{\partial p_{\mathrm{d}}^{\mathrm{w}}}{\partial \boldsymbol{x}} \end{aligned} \tag{9}$$

$$\dot{\boldsymbol{w}}^{\mathrm{a}} = -k^{\mathrm{a}}\frac{\partial h^{\mathrm{a}}}{\partial x} - k^{\mathrm{a}}\frac{\partial\left(h_{\mathrm{d}}^{\mathrm{a}} + h_{\mathrm{ini}}^{\mathrm{a}}\right)}{\partial x} = -k^{\mathrm{a}}\frac{\partial}{\partial x}\left(\frac{p_{\mathrm{d}}^{\mathrm{a}}}{\gamma^{\mathrm{a}}} + h_{\mathrm{ini}}^{\mathrm{a}}\right) = -\frac{k^{\mathrm{a}}}{\gamma^{\mathrm{a}}}\frac{\partial p_{\mathrm{d}}^{\mathrm{a}}}{\partial x} \tag{10}$$

where k^{w} and k^{a} are the coefficients of permeability for water and air, respectively; h^{w} and h^{a} are the total hydraulic head for water and air, respectively; $h_{\mathrm{d}}^{\mathrm{w}}$ and $h_{\mathrm{d}}^{\mathrm{a}}$ are the hydraulic head for water and air caused by excessive pore water pressure (EPWP) and pore air pressure (EPAP), respectively; $h_{\mathrm{ini}}^{\mathrm{w}}$ and $h_{\mathrm{ini}}^{\mathrm{a}}$ are the initial total hydraulic head for water and air, respectively; γ^{w} and γ^{a} are the unit weight of water and air, respectively; $p_{\mathrm{d}}^{\mathrm{w}}(=\gamma^{\mathrm{w}}h_{\mathrm{d}}^{\mathrm{w}})$ and $p_{\mathrm{d}}^{\mathrm{a}}(=\gamma^{\mathrm{a}}h_{\mathrm{d}}^{\mathrm{a}})$ are the EPWP and EPAP, respectively; $\boldsymbol{w}^{\mathrm{w}}$ is the relative displacement vector of liquid phase to solid phase, $\boldsymbol{w}^{\mathrm{a}}$ is the relative displacement vector of air phase to solid phase, and the definitions of them are given as

$$\left.\begin{aligned} \boldsymbol{w}^{\mathrm{w}} &= \boldsymbol{u}^{\mathrm{w}} - \boldsymbol{u}^{\mathrm{s}} \\ \boldsymbol{w}^{\mathrm{a}} &= \boldsymbol{u}^{\mathrm{a}} - \boldsymbol{u}^{\mathrm{s}} \end{aligned}\right\} \tag{11}$$

The mass conservation law for the solid, liquid and air phases in the local form can be written as follows:

$$\left.\begin{aligned} \frac{\partial \overline{\rho}^{\mathrm{s}}}{\partial t} + \mathrm{div}\left(\overline{\rho}^{\mathrm{s}}\boldsymbol{v}^{\mathrm{s}}\right) &= 0 \\ \frac{\partial \overline{\rho}^{\mathrm{w}}}{\partial t} + \mathrm{div}\left(\overline{\rho}^{\mathrm{w}}\boldsymbol{v}^{\mathrm{w}}\right) &= 0 \\ \frac{\partial \overline{\rho}^{\mathrm{a}}}{\partial t} + \mathrm{div}\left(\overline{\rho}^{\mathrm{a}}\boldsymbol{v}^{\mathrm{a}}\right) &= 0 \end{aligned}\right\} \tag{12}$$

The momentum conservation law for the solid, liquid and air phases in the local form can be written as follows:

$$\mathrm{div}(\boldsymbol{T}^{\mathrm{s}}) + \overline{\rho}^{\mathrm{s}}\boldsymbol{b} + \boldsymbol{R} + \boldsymbol{Q} = \boldsymbol{0} \tag{13}$$

$$\mathrm{div}(\boldsymbol{T}^{\mathrm{w}}) + \overline{\rho}^{\mathrm{w}}\boldsymbol{b} - \boldsymbol{R} = \boldsymbol{0} \tag{14}$$

$$\mathrm{div}(\boldsymbol{T}^{\mathrm{a}}) + \overline{\rho}^{\mathrm{a}}\boldsymbol{b} - \boldsymbol{Q} = \boldsymbol{0} \tag{15}$$

where $\boldsymbol{R}$ is the interaction force vector between the liquid and solid phases, $\boldsymbol{Q}$ is the interaction force vector between air and solid phases, and $\boldsymbol{b}$ is the body force vector.

Combining Eqs. (13)–(15), the equilibrium equation of soil–water–air three-phase field theory can be given as

$$\mathrm{div}\boldsymbol{T} + \rho\boldsymbol{b} = \boldsymbol{0} \tag{16}$$

2.2. Continuum equation of liquid phase

Substituting the liquid phase in Eq. (1) into the mass conservation law of Eq. (12), we have

$$(1-n)\frac{\partial \rho^{\mathrm{s}}}{\partial t} + \rho^{\mathrm{s}}\frac{\partial(1-n)}{\partial t} + \rho^{\mathrm{s}}\mathrm{div}\left[(1-n)\boldsymbol{v}^{\mathrm{s}}\right] + (1-n)\boldsymbol{v}^{\mathrm{s}}\mathrm{div}(\rho^{\mathrm{s}}\boldsymbol{I}) = 0 \tag{17}$$

$$nS_{\mathrm{r}}\frac{\partial \rho^{\mathrm{w}}}{\partial t} + \rho^{\mathrm{w}}\frac{\partial(nS_{\mathrm{r}})}{\partial t} + \rho^{\mathrm{w}}\mathrm{div}(nS_{\mathrm{r}}\boldsymbol{v}^{\mathrm{w}}) + nS_{\mathrm{r}}\boldsymbol{v}^{\mathrm{w}}\mathrm{div}(\rho^{\mathrm{w}}\boldsymbol{I}) = 0 \tag{18}$$

Multiplying $S_{\mathrm{r}}\rho^{\mathrm{w}}/\rho^{\mathrm{s}}$ to Eq. (17) and then adding it to Eq. (18), the following equation can be obtained:

$$\begin{aligned} &S_{\mathrm{r}}\rho^{\mathrm{w}}\left[\frac{\partial(1-n)}{\partial t} + \frac{\partial n}{\partial t}\right] + \rho^{\mathrm{w}}\mathrm{div}[nS_{\mathrm{r}}(\boldsymbol{v}^{\mathrm{w}} - \boldsymbol{v}^{\mathrm{s}})] + \\ &S_{\mathrm{r}}\rho^{\mathrm{w}}\mathrm{div}\,\boldsymbol{v}^{\mathrm{s}} + nS_{\mathrm{r}}\left[\frac{\partial \rho^{\mathrm{w}}}{\partial t} + \boldsymbol{v}^{\mathrm{w}}\mathrm{div}(\rho^{\mathrm{w}}\boldsymbol{I})\right] + \\ &n\rho^{\mathrm{w}}\frac{\partial S_{\mathrm{r}}}{\partial t} + S_{\mathrm{r}}(1-n)\frac{\rho^{\mathrm{w}}}{\rho^{\mathrm{s}}}\left[\frac{\partial \rho^{\mathrm{s}}}{\partial t} + \boldsymbol{v}^{\mathrm{s}}\mathrm{div}(\rho^{\mathrm{s}}\boldsymbol{I})\right] = 0 \end{aligned} \tag{19}$$

The first term in Eq. (19) obviously is equal to zero. Considering the assumption (4), the last term equals zero too. Substituting $\mathrm{div}(\boldsymbol{v}) = \mathrm{tr}(\boldsymbol{D})$ and Eq. (11) into Eq. (19) and then dividing $nS_{\mathrm{r}}\rho^{\mathrm{w}}$, the continuum equation of liquid phase can be obtained as the following form:

$$\mathrm{div}(\dot{\boldsymbol{w}}^{\mathrm{w}}) + \frac{\mathrm{tr}(\boldsymbol{D}^{\mathrm{s}})}{n} + \frac{1}{\rho^{\mathrm{w}}}\dot{\rho}^{\mathrm{w}} + \frac{1}{S_{\mathrm{r}}}\dot{S}_{\mathrm{r}} = 0 \tag{20}$$

Considering the influence of temperature θ, the change of water density can be given as

$$\dot{\rho}^{\mathrm{w}} = -\left(\frac{1}{K^{\mathrm{w}}}\dot{p}_{\mathrm{d}}^{\mathrm{w}} + 3\alpha_{\mathrm{T}}^{\mathrm{w}}\dot{\theta}\right)\rho^{\mathrm{w}} \tag{21}$$

where α_T^w is the linear thermal expansion coefficient of liquid phase.

Substituting Eqs. (21) and (9) into Eq. (20), the continuum equation of liquid phase can be written as

$$\frac{\mathrm{tr}(\boldsymbol{D}^s)}{n}-\frac{k^w}{\gamma^w}\mathrm{div}\left[\mathrm{div}\left(p_d^w\boldsymbol{I}\right)\right]-\frac{1}{K^w}\dot{p}_d^w-3\alpha_T^w\dot{\theta}+\frac{1}{S_r}\dot{S}_r=0 \tag{22}$$

2.3. Continuum equation of air phase

Substituting the air phase in Eq. (1) into the mass conservation Eq. (12), we have

$$(1-n)\frac{\partial\rho^s}{\partial t}+\rho^s\frac{\partial(1-n)}{\partial t}+\rho^s\mathrm{div}[(1-n)\boldsymbol{v}^s]+(1-n)\boldsymbol{v}^s\mathrm{div}(\rho^s\boldsymbol{I})=0 \tag{23}$$

$$\begin{aligned}&n(1-S_r)\frac{\partial\rho^a}{\partial t}+\rho^a\frac{\partial[n(1-S_r)]}{\partial t}+\rho^a\mathrm{div}[n(1-S_r)\boldsymbol{v}^a]\\&+n(1-S_r)\boldsymbol{v}^a\mathrm{div}(\rho^a\boldsymbol{I})=0\end{aligned} \tag{24}$$

Multiplying $(1-S_r)\rho^a/\rho^s$ to Eq. (23) and then adding it to Eq. (24), the following equation can be obtained:

$$\begin{aligned}&(1-S_r)\rho^a\left[\frac{\partial(1-n)}{\partial t}+\frac{\partial n}{\partial t}\right]+\rho^a\mathrm{div}[n(1-S_r)(\boldsymbol{v}^a-\boldsymbol{v}^s)]\\&+(1-S_r)\rho^a\mathrm{div}(\boldsymbol{v}^s)+n(1-S_r)\left[\frac{\partial\rho^a}{\partial t}+\boldsymbol{v}^a\mathrm{div}(\rho^a\boldsymbol{I})\right]\\&+n\rho^a\frac{\partial(1-S_r)}{\partial t}+(1-S_r)(1-n)\frac{\rho^a}{\rho^s}\left[\frac{\partial\rho^s}{\partial t}+\boldsymbol{v}^s\mathrm{div}(\rho^s\boldsymbol{I})\right]=0\end{aligned} \tag{25}$$

The first term in Eq. (25) obviously equals zero. Considering the assumption (4), the last term also equals zero. Substituting the relation $\mathrm{div}(\boldsymbol{v})=\mathrm{tr}(\boldsymbol{D})$ and Eq. (11) into Eq. (25) and dividing it with $n(1-S_r)\rho^a$, the continuum equation of air phase can be obtained as the following form:

$$\mathrm{div}(\dot{\boldsymbol{w}}^a)+\frac{\mathrm{tr}(\boldsymbol{D}^s)}{n}+\frac{1}{\rho^a}\dot{\rho}^a-\frac{1}{1-S_r}\dot{S}_r=0 \tag{26}$$

Ignoring the influence of temperature θ, the change of air density can be given as

$$\dot{\rho}^a=-\left(\frac{1}{K^a}\dot{p}_d^a+3\alpha_T^a\dot{\theta}\right)\rho^a \tag{27}$$

where α_T^a is the linear thermal expansion coefficient of air phase.

Substituting Eqs. (10) and (27) into Eq. (26), the continuum equation of air phase can be written as

$$\frac{\mathrm{tr}(\boldsymbol{D}^s)}{n}-\frac{k^a}{\gamma^a}\mathrm{div}\left[\mathrm{div}\left(p_d^a\boldsymbol{I}\right)\right]-\frac{1}{K^a}\dot{p}_d^a-3\alpha_T^a\dot{\theta}-\frac{1}{1-S_r}\dot{S}_r=0 \tag{28a}$$

or

$$\left\{\frac{\mathrm{tr}(\boldsymbol{D}^s)}{n}-\frac{k^a}{\gamma^a}\mathrm{div}\left[\mathrm{div}\left(p_d^a\boldsymbol{I}\right)\right]-\frac{1}{1-S_r}\dot{S}_r\right\}K^a-3\alpha_T^a\dot{\theta}-\dot{p}_d^a=0 \tag{28b}$$

The Eqs. (16), (22) and (28) are the governing equations for the soil–water–air coupling three-phase field theory and are widely used in FEM analysis.

2.4. Equation of energy conservation

Based on the first law of thermodynamics, the following equation can be obtained in the time interval dt:

$$\mathrm{d}U=\mathrm{d}\Phi_{k_t}+\mathrm{d}\Phi_h+E \tag{29}$$

where dU represents the increment of thermal energy; $\mathrm{d}\Phi_{k_t}$ and $\mathrm{d}\Phi_h$ represent the net energy induced by conduction and convection, respectively; and E represents the energy produced by itself such as heat source.

The increment of thermal energy in the region dV can be expressed in the following equation:

$$\begin{aligned}\mathrm{d}U=&(1-n)(c\rho)^s\mathrm{d}V\frac{\partial\theta}{\partial t}\mathrm{d}t+nS_r(c\rho)^w\mathrm{d}V\frac{\partial\theta}{\partial t}\mathrm{d}t\\&+n(1-S_r)(c\rho)^a\mathrm{d}V\frac{\partial\theta}{\partial t}\mathrm{d}t=(\overline{c\rho})\frac{\partial T}{\partial t}\mathrm{d}V\mathrm{d}t\end{aligned} \tag{30}$$

where

$$\overline{\rho c}=(1-n)(c\rho)^s+nS_r(c\rho)^w+n(1-S_r)(c\rho)^a$$

where c is the specific heat.

The net energy of $\mathrm{d}\Phi_{k_t}$ can be expressed as

$$\begin{aligned}\mathrm{d}\Phi_{k_t}=&(1-n)[-\mathrm{div}(\boldsymbol{q}^s)]\mathrm{d}V+nS_r[-\mathrm{div}(\boldsymbol{q}^w)]\mathrm{d}V\\&+n(1-S_r)[-\mathrm{div}(\boldsymbol{q}^a)]\mathrm{d}V\end{aligned} \tag{31}$$

where $\boldsymbol{q}$ is the heat flux.

According to Fourier's law, Eq. (31) can be rewritten as

$$\begin{aligned}\mathrm{d}\Phi_{k_t}=&(1-n)k_t^s\mathrm{div}(\mathrm{div}\theta)\mathrm{d}V\mathrm{d}t+nS_rk_t^w\mathrm{div}(\mathrm{div}\theta)\mathrm{d}V\mathrm{d}t\\&+n(1-S_r)k_t^a\mathrm{div}(\mathrm{div}\theta)\mathrm{d}V\mathrm{d}t=\bar{k}_t\mathrm{div}(\mathrm{div}\theta)\mathrm{d}V\mathrm{d}t\end{aligned} \tag{32}$$

where $\bar{k}_t=(1-n)k_t^s+nS_rk_t^w+n(1-S_r)k_t^a$ is the average heat conductivity of the three-phase soil material.

Similar to $\mathrm{d}\Phi_{k_t}$, $\mathrm{d}\Phi_h$ also can be expressed as

$$\begin{aligned}\mathrm{d}\Phi_h=&-nS_r(\rho c)^w\mathrm{div}(\boldsymbol{v}^w\theta)\mathrm{d}V\mathrm{d}t-n(1-S_r)(\rho c)^a\mathrm{div}(\boldsymbol{v}^a\theta)\mathrm{d}V\mathrm{d}t\\=&-nS_r(\rho c)^w\boldsymbol{v}^w\mathrm{div}(\theta)\mathrm{d}V\mathrm{d}t-n(1-S_r)(\rho c)^a\boldsymbol{v}^a\mathrm{div}(\theta)\mathrm{d}V\mathrm{d}t\end{aligned} \tag{33}$$

in the derivation, and the term $\mathrm{div}(\boldsymbol{v})$ can be regarded as zero when the gradient of velocity is very small in impermeable rock.

Substituting Eqs. (30), (32) and (33) into Eq. (29), the equation of energy conservation can be obtained:

$$\begin{aligned}&(\overline{\rho c})\frac{\partial\theta}{\partial t}+nS_r(\rho c)^w\boldsymbol{v}^w\mathrm{div}(\theta)+n(1-S_r)(\rho c)^a\boldsymbol{v}^a\mathrm{div}(\theta)\\&=\bar{k}_t\mathrm{div}[\mathrm{div}(\theta)]+E\end{aligned} \tag{34}$$

It is worth noting that the thermal energy conservation is not fully coupled with mechanical behavior in this scheme, because the energy dissipation due to the plastic deformation described by the constitutive model (Xiong, 2013) is not included in the above

conservation equation, though it might be very small and can be neglected in terms of engineering sensor if compared with the heat energy produced by nuclear waste.

2.5. Discretization of equilibrium equation in space and time

In Eq. (16), Cauchy stress $\boldsymbol{T}$ is defined in the coordinate system of current time, i.e. the coordinate system in which the object has deformed. In FEM analysis of finite deformation, however, stress calculation is all based on the initial reference coordinate system so that it is necessary to use the nominal stress, such as the first Piola–Kirchhoff stress, instead of the Cauchy stress.

By using the first Piola–Kirchhoff stress and virtual work theorem, the weak form of the equilibrium equation in an arbitrary region V can be expressed as

$$\int_V (\mathrm{div}\boldsymbol{\Pi} + \rho\boldsymbol{b})\delta\dot{\boldsymbol{u}}^{\mathrm{s}}\mathrm{d}V = 0 \tag{35}$$

where $\delta\dot{\boldsymbol{u}}^{\mathrm{s}}$ is the arbitrary virtual velocity vector of solid phase, and $\boldsymbol{\Pi}$ is the first Piola–Kirchhoff stress tensor. It is in relation with the Cauchy stress tensor by

$$\boldsymbol{\Pi} = J\boldsymbol{T}\boldsymbol{F}^{-\mathrm{T}} \tag{36}$$

where $J = \det \boldsymbol{F}$ is the volume change rate, and $\boldsymbol{F}$ is the deformation gradient tensor.

Integrating Eq. (35), we have

$$\int_S \boldsymbol{\Pi}\boldsymbol{n}\delta\dot{\boldsymbol{u}}^{\mathrm{s}}\mathrm{d}S + \int_V \rho\boldsymbol{b}\,\delta\dot{\boldsymbol{u}}^{\mathrm{s}}\mathrm{d}V = \int_V \boldsymbol{\Pi}\delta\boldsymbol{L}\mathrm{d}V \tag{37}$$

where $\delta\boldsymbol{L}$ is the arbitrary virtual velocity gradient, S is the close surface of region V, and $\boldsymbol{n}$ is the outward unit normal vector of the surface S. Considering boundary condition, the surface force vector $\boldsymbol{t}$ can be calculated from the Cauchy equation:

$$\boldsymbol{t} = \boldsymbol{\Pi}\boldsymbol{n} \tag{38}$$

Substituting Eq. (38) into Eq. (37), the following equation can be obtained:

$$\int_V \boldsymbol{\Pi}\,\delta\boldsymbol{L}\mathrm{d}V = \int_V \rho\boldsymbol{b}\delta\dot{\boldsymbol{u}}^{\mathrm{s}}\mathrm{d}V + \int_S \boldsymbol{t}\delta\dot{\boldsymbol{u}}^{\mathrm{s}}\mathrm{d}S \tag{39}$$

The incremental form of the above equation in finite element scheme can be written as follows:

$$\int_V \Delta t\dot{\boldsymbol{\Pi}}_{|t+\Delta t}\delta\boldsymbol{L}\mathrm{d}V = \int_V \rho\Delta\boldsymbol{b}\delta\dot{\boldsymbol{u}}^{\mathrm{s}}\mathrm{d}V + \int_S \Delta\boldsymbol{t}\delta\dot{\boldsymbol{u}}^{\mathrm{s}}\mathrm{d}S \tag{40}$$

The stress rate at the current time $t + \Delta t$ can be expressed according to the work by Yatomi et al. (1989) as

$$\dot{\boldsymbol{\Pi}}_{|t+\Delta t} = \left(\boldsymbol{\Pi}_{|t+\Delta t} - \boldsymbol{\Pi}_{|t}\right)/\Delta t = \Delta\boldsymbol{\Pi}_{|t+\Delta t}/\Delta t = \overset{\nabla}{\dot{\boldsymbol{T}}} + (\mathrm{tr}\boldsymbol{D})\boldsymbol{T} - \boldsymbol{T}\boldsymbol{L}^{\mathrm{T}} \tag{41}$$

On the other hand, from the definitions, the Jaumann stress rate tensor and Green–Naghdi stress rate tensor are listed below.

Jaumann stress rate tensor is

$$\overset{\nabla}{\dot{\boldsymbol{T}}} = \dot{\boldsymbol{T}}' - \boldsymbol{W}\boldsymbol{T}' + \boldsymbol{T}'\boldsymbol{W} \tag{42}$$

Green–Naghdi stress rate tensor is

$$\mathring{\dot{\boldsymbol{T}}} = \dot{\boldsymbol{T}}' - \boldsymbol{\Omega}\dot{\boldsymbol{T}}' + \dot{\boldsymbol{T}}'\boldsymbol{\Omega} \tag{43}$$

We can obtain the following equations by substituting Eq. (42) or (43) into Eq. (41):

$$\dot{\boldsymbol{\Pi}} = \overset{\nabla}{\dot{\boldsymbol{T}}} + (\mathrm{tr}\boldsymbol{D})\boldsymbol{T} - \boldsymbol{T}\boldsymbol{L}^{\mathrm{T}} + (\boldsymbol{W}\boldsymbol{T}' - \boldsymbol{T}'\boldsymbol{W}) + [S_{\mathrm{r}}p^{\mathrm{w}}]^{\bullet}\boldsymbol{I} + [(1-S_{\mathrm{r}})p^{\mathrm{a}}]^{\bullet}\boldsymbol{I} \tag{44}$$

and

$$\dot{\boldsymbol{\Pi}} = \mathring{\dot{\boldsymbol{T}}} + (\mathrm{tr}\boldsymbol{D})\boldsymbol{T} - \boldsymbol{T}\boldsymbol{L}^{\mathrm{T}} + (\boldsymbol{\Omega}\boldsymbol{T}' - \boldsymbol{T}'\boldsymbol{\Omega}) + [S_{\mathrm{r}}p^{\mathrm{w}}]^{\bullet}\boldsymbol{I} + [(1-S_{\mathrm{r}})p^{\mathrm{a}}]^{\bullet}\boldsymbol{I} \tag{45}$$

where $\boldsymbol{W} = (\boldsymbol{L} - \boldsymbol{L}^{\mathrm{T}})/2$ is the spin tensor, $\boldsymbol{\Omega} = \dot{\boldsymbol{R}}\boldsymbol{R}^{\mathrm{T}}$ is the rigid body spin tensor, and $[\,]^{\bullet}$ represents the material time derivation.

Eqs. (44) and (45) can be integrated as

$$\begin{aligned}\int_V \Delta t\dot{\boldsymbol{\Pi}}\delta\boldsymbol{L}\mathrm{d}V = &\int_V \Delta t\left\{\overset{\nabla}{\dot{\boldsymbol{T}}} + (\mathrm{tr}\boldsymbol{D})\boldsymbol{T} - \boldsymbol{T}\boldsymbol{L}^{\mathrm{T}}\right\}\delta\boldsymbol{L}\mathrm{d}V\\ &+\int_V \Delta t(\boldsymbol{W}\boldsymbol{T}' - \boldsymbol{T}'\boldsymbol{W})\delta\boldsymbol{L}\mathrm{d}V + \int_V \Delta t\{[S_{\mathrm{r}}p^{\mathrm{w}}]^{\bullet}\boldsymbol{I}\\ &+[(1-S_{\mathrm{r}})p^{\mathrm{a}}]^{\bullet}\boldsymbol{I}\}\delta\boldsymbol{L}\mathrm{d}V = \Delta t\int_V \overset{\nabla}{\dot{\boldsymbol{T}}}\delta\boldsymbol{D}\mathrm{d}V\\ &+\Delta t\int_V \left[(\mathrm{tr}\boldsymbol{D})\boldsymbol{T} - \boldsymbol{T}\boldsymbol{L}^{\mathrm{T}}\right]\delta\boldsymbol{L}\mathrm{d}V + \Delta t\int_V (\boldsymbol{W}\boldsymbol{T}' - \boldsymbol{T}'\boldsymbol{W})\delta\boldsymbol{L}\mathrm{d}V\\ &+\Delta t\int_V [S_{\mathrm{r}}\dot{p}^{\mathrm{w}}\boldsymbol{I} + (1-S_{\mathrm{r}})\dot{p}^{\mathrm{a}}\boldsymbol{I}]\delta\boldsymbol{L}\mathrm{d}V\end{aligned} \tag{46}$$

and

$$\begin{aligned}\int_V \Delta t\dot{\boldsymbol{\Pi}}\delta\boldsymbol{L}\mathrm{d}V = &\int_V \Delta t\left[\mathring{\dot{\boldsymbol{T}}} + (\mathrm{tr}\boldsymbol{D})\boldsymbol{T} - \boldsymbol{T}\boldsymbol{L}^{\mathrm{T}}\right]\delta\boldsymbol{L}\mathrm{d}V\\ &+\int_V \Delta t(\boldsymbol{\Omega}\boldsymbol{T}' - \boldsymbol{T}'\boldsymbol{\Omega})\delta\boldsymbol{L}\mathrm{d}V + \int_V \Delta t\{[S_{\mathrm{r}}p^{\mathrm{w}}]^{\bullet}\boldsymbol{I}\\ &+[(1-S_{\mathrm{r}})p^{\mathrm{a}}]^{\bullet}\boldsymbol{I}\}\delta\boldsymbol{L}\mathrm{d}V = \Delta t\int_V \mathring{\dot{\boldsymbol{T}}}\delta\boldsymbol{D}\mathrm{d}V\\ &+\Delta t\int_V \left[(\mathrm{tr}\boldsymbol{D})\boldsymbol{T} - \boldsymbol{T}\boldsymbol{L}^{\mathrm{T}}\right]\delta\boldsymbol{L}\mathrm{d}V\\ &+\Delta t\int_V (\boldsymbol{\Omega}\boldsymbol{T}' - \boldsymbol{T}'\boldsymbol{\Omega})\delta\boldsymbol{L}\mathrm{d}V + \Delta t\int_V [S_{\mathrm{r}}\dot{p}^{\mathrm{w}}\boldsymbol{I}\\ &+(1-S_{\mathrm{r}})\dot{p}^{\mathrm{a}}\boldsymbol{I}]\delta\boldsymbol{L}\mathrm{d}V\end{aligned} \tag{47}$$

We use different shape functions for displacement and pore pressures (water and air) in FEM discretization. The variables of displacement are given at the nodes and the variables of pore pressures are given at the gravitational center, respectively.

$\vec{\dot{u}}_{\mathrm{N}}$ is the nodal displacement velocity vector of all nodes in one element. The displacement velocity vector (virtual displacement vector) at any arbitrary point within this element, $\vec{\dot{u}}^{\mathrm{s}}$ ($\delta\vec{\dot{u}}^{\mathrm{s}}$), can then be expressed by the nodal displacement vector $\vec{\dot{u}}_{\mathrm{N}}$ as

$$\vec{u}^{s} = [N]\vec{u}_N \tag{48}$$

$$\delta\vec{u}^{s} = [N]\delta\vec{u}_N \tag{49}$$

where $[N]$ is the matrix of the shape function.

The strain rate vector at any arbitrary point within an element can be written as

$$\vec{\boldsymbol{D}} = [L]\vec{u}^{s} = [L][N]\vec{u}_N = [B]\vec{u}_N \tag{50}$$

$$\mathrm{tr}\boldsymbol{D} = [\overline{M}][L][N]\vec{u}_N = \vec{B}_v^{T}\vec{u}_N = \vec{u}_N^{T}\vec{B}_v \tag{51}$$

The velocity gradient vector of any arbitrary point within an element can be changed to vector form:

$$\vec{L} = [B_{NL}]\vec{u}_N \tag{52}$$

On the one hand, in the work by Xiong (2013), a thermo-elastoplastic constitutive model for unsaturated/saturated soil was newly proposed based on an elastoplastic constitutive model for unsaturated soil (Zhang and Ikariya, 2011) and a thermo-elastoplastic constitutive model for saturated soil (Zhang and Zhang, 2009; Zhang et al., 2012). Based on the new model, Eqs. (42) and (43) can be rewritten with the vector forms as

$$\overset{\nabla}{\boldsymbol{T}} = [D]^{ep}[B]\Delta\vec{u}_N - E^{RFS}\Delta\dot{S}_r - \alpha_T^s[D]^{ep}[M][N]\dot{\theta}_N \tag{53a}$$

or

$$\mathring{\boldsymbol{T}} = [D]^{ep}[B]\Delta\vec{u}_N - E^{RFS}\Delta\dot{S}_r - \alpha_T^s[D]^{ep}[M][N]\dot{\theta}_N \tag{53b}$$

$$E^{RFS} = \frac{1}{C_p}\frac{Q}{1+e_0}\frac{1}{\tilde{D}}[D]^{e}\frac{\partial f}{\partial\sigma} \tag{54}$$

where $[D]^e$ and $[D]^{ep}$ are the elastic and elastoplastic matrix stiffness respectively (see Appendix and Xiong (2013)); α_T^s is the linear thermal expansion of soil; $[M]^T = \{1, 1, 1, 0, 0, 0\}$; and $\dot{\theta}_N = (\theta_{N|t+\Delta t} - \theta_{N|t})/\Delta t = \Delta\theta_{N|t+\Delta t}/\Delta t$ is the matrix of the nodal incremental temperature.

2.5.1. Jaumann stress rate tensor

Expressing the items in Eq. (46) with vector form, we have

$$\begin{aligned}\int_V \Delta t\dot{\boldsymbol{\Pi}}\delta\boldsymbol{L}\mathrm{d}V =& \Delta t\int_V \overset{\nabla}{\boldsymbol{T}}\delta\boldsymbol{D}\mathrm{d}V + \Delta t\int_V\left[(\mathrm{tr}\boldsymbol{D})\boldsymbol{T} - \boldsymbol{T}\boldsymbol{L}^{T} + \boldsymbol{W}\boldsymbol{T}' - \boldsymbol{T}'\boldsymbol{W}\right]\\ &\delta\boldsymbol{L}\mathrm{d}V + \Delta t\int_V\{[S_r p^w]^{\bullet}\boldsymbol{I} + [(1-S_r)p^a]^{\bullet}\boldsymbol{I}\}\delta\boldsymbol{L}\mathrm{d}V\\ =& \Delta t\int_V \delta\vec{u}_N^{T}[B]^{T}[D]^{ep}[B]\vec{u}_N\mathrm{d}V - \Delta t\int_V \delta\vec{u}_N^{T}[B]^{T}\vec{E}^{RFS}\\ &\times\mathrm{d}V\Delta\dot{S}_r + \Delta t\int_V \delta\vec{u}_N^{T}[B_{NL}]^{T}\left[T^*\right][B_{NL}]\vec{u}_N\mathrm{d}V\\ &-\left(\Delta t\alpha_T^s\int_V \delta\vec{u}_N^{T}[B]^{T}[D]^{ep}[M][N]\mathrm{d}V\right)\dot{\theta}_N\\ &+\Delta t\int_V \delta\vec{u}_N^{T}\vec{B}_v\{[S_r p^w]^{\bullet} + [(1-S_r)p^a]^{\bullet}\}\mathrm{d}V\end{aligned} \tag{55}$$

where

$$\left[(\mathrm{tr}\boldsymbol{D})\boldsymbol{T} - \boldsymbol{T}\boldsymbol{L}^{T} + \boldsymbol{W}\boldsymbol{T}' - \boldsymbol{T}'\boldsymbol{W}\right]\delta\boldsymbol{L} = \delta\vec{u}_N^{T}[B_{NL}]^{T}\left[T^*\right][B_{NL}]\vec{u}_N$$

Moreover, the following items can be easily obtained:

$$\int_V \rho\Delta\boldsymbol{b}\delta\boldsymbol{u}^{s}\mathrm{d}V = \int_V \delta\vec{u}_N[N]^{T}\rho\Delta\vec{b}\,\mathrm{d}V \tag{56}$$

$$\int_S \Delta\boldsymbol{t}\delta\boldsymbol{u}^{s}\mathrm{d}S = \int_S \delta\vec{u}_N[N]^{T}\Delta\vec{t}\,\mathrm{d}S \tag{57}$$

Substituting Eqs. (53a or 53b) to (57) into Eq. (40), and because the virtual displacement velocity is arbitrary and pore pressure is taken as a constant value within one element in discretization, the following equation can be obtained with vector form:

$$\begin{aligned}&\Delta t\int_V [B]^{T}[D]^{ep}[B]\vec{u}_N\mathrm{d}V - \Delta t\int_V [B]^{T}\vec{E}^{RFS}\mathrm{d}V\Delta\dot{S}_r\\ &+\Delta t\int_V [B_{NL}]^{T}\left[T^*\right][B_{NL}]\vec{u}_N\mathrm{d}V + \Delta t\int_V \vec{B}_v\mathrm{d}V\{[S_r p^w_{dE}]^{\bullet}\\ &+[(1-S_r)p^a_{dE}]^{\bullet}\} = \int_V \rho[N]^{T}\Delta\vec{b}\,\mathrm{d}V + \int_S [N]^{T}\Delta\vec{t}\,\mathrm{d}S\\ &+\left(\Delta t\alpha_T^s\int_V [B]^{T}[D]^{ep}[M][N]\mathrm{d}V\right)\dot{\theta}_N\end{aligned} \tag{58}$$

where p^a_{dE} and p^w_{dE} are the constant EPWP and EPAP within one element in discretization, respectively.

In nonlinear FEM analysis, it is necessary to do incremental calculation so that the above equation is changed to incremental form:

$$\begin{aligned}&\int_V [B]^{T}[D]^{ep}[B]\Delta\vec{u}_N\mathrm{d}V - \int_V [B]^{T}\vec{E}^{RFS}\mathrm{d}V\Delta S_r\\ &+\int_V [B_{NL}]^{T}\left[T^*\right][B_{NL}]\Delta\vec{u}_N\mathrm{d}V + \int_V \vec{B}_v\mathrm{d}V\{\Delta(S_r p^w_{dE})\\ &+\Delta[(1-S_r)p^a_{dE}]\} = \int_V \rho[N]^{T}\Delta\vec{b}\,\mathrm{d}V + \int_S [N]^{T}\Delta\vec{t}\,\mathrm{d}S\\ &+\left(\alpha_T^s\int_V [B]^{T}[D]^{ep}[M][N]\mathrm{d}V\right)\Delta\theta_N\end{aligned} \tag{59}$$

We can also define the following equations:

$$\Delta\vec{F} = \int_V \rho[N]^{T}\Delta\vec{b}\,\mathrm{d}V + \int_S [N]^{T}\Delta\vec{t}\,\mathrm{d}S \tag{60}$$

$$[K] = \int_V [B]^{T}[D]^{ep}[B]\mathrm{d}V + \int_V [B_{NL}]^{T}\left[T^*\right][B_{NL}]\mathrm{d}V \tag{61}$$

$$\left.\begin{aligned}\overrightarrow{K}_{\mathrm{Sat}} &= \int_V [B]^{\mathrm{T}}\overrightarrow{E}^{\mathrm{RFS}}\mathrm{d}V\\ \overrightarrow{K}_{\mathrm{v}} &= \int_V \overrightarrow{B}_{\mathrm{v}}\mathrm{d}V\\ \overrightarrow{F}_{\mathrm{T}} &= \alpha_{\mathrm{T}}^{\mathrm{s}}\int_V [B]^{\mathrm{T}}[D]^{\mathrm{ep}}[M][N]\mathrm{d}V\end{aligned}\right\} \tag{62}$$

2.5.2. Green–Naghdi stress rate tensor

Expressing the items in Eq. (47) with vector form, we have

$$\int_V \Delta t\dot{\boldsymbol{I}}\boldsymbol{I}\delta\boldsymbol{L}\mathrm{d}V = \Delta t\int_V \dot{\boldsymbol{T}}\delta\boldsymbol{D}\mathrm{d}V + \Delta t\int_V \left[(\mathrm{tr}\boldsymbol{D})\boldsymbol{T} - \boldsymbol{T}\boldsymbol{L}^{\mathrm{T}}\right]\delta\boldsymbol{L}\mathrm{d}V$$

$$+\Delta t\int_V (\boldsymbol{\Omega}\boldsymbol{T}' - \boldsymbol{T}'\boldsymbol{\Omega})\delta\boldsymbol{D}\mathrm{d}V + \Delta t\int_V \{[S_{\mathrm{r}}p^{\mathrm{w}}]^{\bullet}\boldsymbol{I} + [(1-S_{\mathrm{r}})p^{\mathrm{a}}]^{\bullet}\boldsymbol{I}\}\delta\boldsymbol{L}\mathrm{d}V$$

$$= \Delta t\int_V \delta\overrightarrow{\dot{u}}_{\mathrm{N}}^{\mathrm{T}}[B]^{\mathrm{T}}[D]^{\mathrm{ep}}[B]\overrightarrow{\dot{u}}_{\mathrm{N}}\mathrm{d}V - \Delta t\int_V \delta\overrightarrow{\dot{u}}_{\mathrm{N}}^{\mathrm{T}}[B]^{\mathrm{T}}\overrightarrow{E}^{\mathrm{RFS}}\mathrm{d}V\Delta\dot{S}_{\mathrm{r}}$$

$$+\Delta t\int_V \delta\overrightarrow{\dot{u}}_{\mathrm{N}}^{\mathrm{T}}[B_{\mathrm{NL}}]^{\mathrm{T}}\left[T^{**}\right][B_{\mathrm{NL}}]\overrightarrow{\dot{u}}_{\mathrm{N}}\mathrm{d}V + \Delta t\int_V \delta\overrightarrow{\dot{u}}_{\mathrm{N}}^{\mathrm{T}}[B]^{\mathrm{T}}[T_{\Omega}]\mathrm{d}V$$

$$+\Delta t\int_V \delta\overrightarrow{\dot{u}}_{\mathrm{N}}^{\mathrm{T}}\overrightarrow{B}_{\mathrm{v}}\{[S_{\mathrm{r}}p^{\mathrm{w}}]^{\bullet} + [(1-S_{\mathrm{r}})p^{\mathrm{a}}]^{\bullet}\}\mathrm{d}V$$

$$-\left(\Delta t\alpha_{\mathrm{T}}^{\mathrm{s}}\int_V \delta\overrightarrow{\dot{u}}_{\mathrm{N}}^{\mathrm{T}}[B]^{\mathrm{T}}[D]^{\mathrm{ep}}[M][N]\mathrm{d}V\right)\dot{\theta}_{\mathrm{N}} \tag{63}$$

where

$$\left[(\mathrm{tr}\boldsymbol{D})\boldsymbol{T} - \boldsymbol{T}\boldsymbol{L}^{\mathrm{T}}\right]\delta\boldsymbol{L} = \delta\overrightarrow{\dot{u}}_{\mathrm{N}}^{\mathrm{T}}[B_{\mathrm{NL}}]^{\mathrm{T}}\left[T^{**}\right][B_{\mathrm{NL}}]\overrightarrow{\dot{u}}_{\mathrm{N}}$$

$$(\boldsymbol{\Omega}\boldsymbol{T}' - \boldsymbol{T}'\boldsymbol{\Omega})\delta\boldsymbol{D} = \delta\overrightarrow{\dot{u}}_{\mathrm{N}}^{\mathrm{T}}[B]^{\mathrm{T}}[T_{\Omega}]$$

Substituting Eqs. (53b), (56) and (57) into Eq. (40), the following equation with incremental form can be obtained:

$$\int_V [B]^{\mathrm{T}}[D]^{\mathrm{ep}}[B]\Delta\overrightarrow{u}_{\mathrm{N}}\mathrm{d}V - \int_V [B]^{\mathrm{T}}\overrightarrow{E}^{\mathrm{RFS}}\mathrm{d}V\Delta S_{\mathrm{r}}$$
$$+\int_V [B_{\mathrm{NL}}]^{\mathrm{T}}\left[T^{**}\right][B_{\mathrm{NL}}]\Delta\overrightarrow{u}_{\mathrm{N}}\mathrm{d}V + \int_V \overrightarrow{B}_{\mathrm{v}}\mathrm{d}V\{\Delta(S_{\mathrm{r}}p_{\mathrm{dE}}^{\mathrm{w}})$$
$$+\Delta\left[(1-S_{\mathrm{r}})p_{\mathrm{dE}}^{\mathrm{a}}\right]\} = \int_V \rho[N]^{\mathrm{T}}\Delta\overrightarrow{b}\mathrm{d}V + \int_S [N]^{\mathrm{T}}\Delta\overrightarrow{t}\mathrm{d}S$$
$$-\Delta t\int_V [B]^{\mathrm{T}}\left[T_{\Omega}'\right]\mathrm{d}V + \left(\alpha_{\mathrm{T}}^{\mathrm{s}}\int_V [B]^{\mathrm{T}}[D]^{\mathrm{ep}}[M][N]\mathrm{d}V\right)\Delta\theta_{\mathrm{N}} \tag{64}$$

We can define the following equations:

$$\Delta\overrightarrow{F} = \int_V \rho[N]^{\mathrm{T}}\Delta\overrightarrow{b}\mathrm{d}V + \int_S [N]^{\mathrm{T}}\Delta\overrightarrow{t}\mathrm{d}S - \Delta t\int_V [B]^{\mathrm{T}}\left[T_{\Omega}'\right]\mathrm{d}V \tag{65}$$

$$[K] = \int_V [B]^{\mathrm{T}}[D]^{\mathrm{ep}}[B]\mathrm{d}V + \int_V [B_{\mathrm{NL}}]^{\mathrm{T}}\left[T^{**}\right][B_{\mathrm{NL}}]\mathrm{d}V \tag{66}$$

By using the Eqs. (60)–(62), Eq. (59) or (64) can be rewritten as

$$[K]\Delta\overrightarrow{u}_{\mathrm{N}} - \overrightarrow{K}_{\mathrm{Sat}}\Delta S_{\mathrm{r}} + \overrightarrow{K}_{\mathrm{v}}\Delta(S_{\mathrm{r}}p_{\mathrm{dE}}^{\mathrm{w}}) + \overrightarrow{K}_{\mathrm{v}}\Delta\left[(1-S_{\mathrm{r}})p_{\mathrm{dE}}^{\mathrm{a}}\right]$$
$$= \Delta\overrightarrow{F} + \overrightarrow{F}_{\mathrm{T}}\Delta\theta_{\mathrm{N}} \tag{67}$$

The incremental forms of $\Delta(S_{\mathrm{r}}p_{\mathrm{dE}}^{\mathrm{w}})$ and $\Delta[(1-S_{\mathrm{r}})p_{\mathrm{dE}}^{\mathrm{a}}]$ are approximated as

$$\Delta(S_{\mathrm{r}}p_{\mathrm{dE}}^{\mathrm{w}}) = \Delta S_{\mathrm{r}}p_{\mathrm{dE}}^{\mathrm{w}} + S_{\mathrm{r}}\Delta p_{\mathrm{dE}}^{\mathrm{w}} = \Delta S_{\mathrm{r}|t+\Delta t}p_{\mathrm{dE}|t}^{\mathrm{w}} + S_{\mathrm{r}|t}\Delta p_{\mathrm{dE}|t+\Delta t}^{\mathrm{w}} \tag{68}$$

$$\Delta\left[(1-S_{\mathrm{r}})p_{\mathrm{dE}}^{\mathrm{w}}\right] = \left(1-S_{\mathrm{r}|t}\right)\Delta p_{\mathrm{dE}|t+\Delta t}^{\mathrm{a}} - \Delta S_{\mathrm{r}|t+\Delta t}p_{\mathrm{dE}|t}^{\mathrm{a}} \tag{69}$$

$$\Delta S_{\mathrm{r}|t+\Delta t} = S_{\mathrm{r}|t+\Delta t} - S_{\mathrm{r}|t} \tag{70}$$

On the other hand, in the work by Zhang and Ikariya (2011), a new moisture characteristics curve (MCC) is also proposed, where the relationship between the incremental suction and saturation is expressed as

$$\Delta S_{\mathrm{r}|t+\Delta t} = \boldsymbol{k}_{\mathrm{s}}^{-1}\Delta s_{|t+\Delta t} \tag{71}$$

$$\Delta s_{|t+\Delta t} = \left(p_{\mathrm{dE}|t+\Delta t}^{\mathrm{a}} - p_{\mathrm{dE}|t+\Delta t}^{\mathrm{w}}\right) - \left(p_{\mathrm{dE}|t}^{\mathrm{a}} - p_{\mathrm{dE}|t}^{\mathrm{w}}\right)$$
$$= \Delta p_{\mathrm{dE}|t+\Delta t}^{\mathrm{a}} - \Delta p_{\mathrm{dE}|t+\Delta t}^{\mathrm{w}} \tag{72}$$

where $\boldsymbol{k}_{\mathrm{s}}^{-1}$ is the stiffness of saturation–suction relation.

Substituting Eq. (68)–(72) into Eq. (67), the equilibrium equation discretized in space and time can be obtained:

$$[K]\Delta\overrightarrow{u}_{\mathrm{N}|t+\Delta t} + \left[\overrightarrow{K}_{\mathrm{v}}S_{\mathrm{r}|t} - \left(\overrightarrow{K}_{\mathrm{v}}p_{\mathrm{dE}|t}^{\mathrm{w}} - \overrightarrow{K}_{\mathrm{v}}p_{\mathrm{dE}|t}^{\mathrm{a}} - \overrightarrow{K}_{\mathrm{Sat}}\right)\boldsymbol{k}_{\mathrm{s}}^{-1}\right]p_{\mathrm{dE}|t+\Delta t}^{\mathrm{w}}$$
$$+\left\{\left(1-S_{\mathrm{r}|t}\right)\overrightarrow{K}_{\mathrm{v}} + \left(\overrightarrow{K}_{\mathrm{v}}p_{\mathrm{dE}|t}^{\mathrm{w}} - \overrightarrow{K}_{\mathrm{v}}p_{\mathrm{dE}|t}^{\mathrm{a}} - \overrightarrow{K}_{\mathrm{Sat}}\right)\boldsymbol{k}_{\mathrm{s}}^{-1}\right\}p_{\mathrm{dE}|t+\Delta t}^{\mathrm{a}}$$
$$= \Delta\overrightarrow{F}_{|t+\Delta t} + \overrightarrow{F}_{\mathrm{T}}\Delta\theta_{\mathrm{N}|t+\Delta t}$$
$$+\left[\overrightarrow{K}_{\mathrm{v}}S_{\mathrm{r}|t} - \left(\overrightarrow{K}_{\mathrm{v}}p_{\mathrm{dE}|t}^{\mathrm{w}} - \overrightarrow{K}_{\mathrm{v}}p_{\mathrm{dE}|t}^{\mathrm{a}} - \overrightarrow{K}_{\mathrm{Sat}}\right)\boldsymbol{k}_{\mathrm{s}}^{-1}\right]p_{\mathrm{dE}|t}^{\mathrm{w}}$$
$$+\left\{\left(1-S_{\mathrm{r}|t}\right)\overrightarrow{K}_{\mathrm{v}} + \left(\overrightarrow{K}_{\mathrm{v}}p_{\mathrm{dE}|t}^{\mathrm{w}} - \overrightarrow{K}_{\mathrm{v}}p_{\mathrm{dE}|t}^{\mathrm{a}} - \overrightarrow{K}_{\mathrm{Sat}}\right)\boldsymbol{k}_{\mathrm{s}}^{-1}\right\}p_{\mathrm{dE}|t}^{\mathrm{a}} \tag{73}$$

By defining the following equation:

$$\overrightarrow{I}_{\mathrm{Sat}}^{\mathrm{w}} = \overrightarrow{K}_{\mathrm{v}}S_{\mathrm{r}|t} - \left(\overrightarrow{K}_{\mathrm{v}}p_{\mathrm{dE}|t}^{\mathrm{w}} - \overrightarrow{K}_{\mathrm{v}}p_{\mathrm{dE}|t}^{\mathrm{a}} - \overrightarrow{K}_{\mathrm{Sat}}\right)\boldsymbol{k}_{\mathrm{s}}^{-1} \tag{74}$$

$$\overrightarrow{I}_{\mathrm{Sat}}^{\mathrm{a}} = \left(1-S_{\mathrm{r}|t}\right)\overrightarrow{K}_{\mathrm{v}} + \left(\overrightarrow{K}_{\mathrm{v}}p_{\mathrm{dE}|t}^{\mathrm{w}} - \overrightarrow{K}_{\mathrm{v}}p_{\mathrm{dE}|t}^{\mathrm{a}} - \overrightarrow{K}_{\mathrm{Sat}}\right)\boldsymbol{k}_{\mathrm{s}}^{-1} \tag{75}$$

Eq. (73) can finally be rewritten as

$$[K]\Delta\overrightarrow{u}_{\mathrm{N}|t+\Delta t} + \overrightarrow{I}_{\mathrm{Sat}}^{\mathrm{w}}p_{\mathrm{dE}|t+\Delta t}^{\mathrm{w}} + \overrightarrow{I}_{\mathrm{Sat}}^{\mathrm{a}}p_{\mathrm{dE}|t+\Delta t}^{\mathrm{a}}$$
$$= \Delta\overrightarrow{F}_{|t+\Delta t} + \overrightarrow{F}_{\mathrm{T}}\Delta\theta_{\mathrm{N}|t+\Delta t} + \overrightarrow{I}_{\mathrm{Sat}}^{\mathrm{w}}p_{\mathrm{dE}|t}^{\mathrm{w}} + \overrightarrow{I}_{\mathrm{Sat}}^{\mathrm{a}}p_{\mathrm{dE}|t}^{\mathrm{a}} \tag{76}$$

2.6. Discretization of continuum equation of liquid phase in space and time

The discretization of continuum equation of liquid phase can be implemented by the same way used in the previous section.

From Eq. (51), it can be known:

$$\mathrm{tr}\boldsymbol{D} = \overrightarrow{B}_{\mathrm{v}}^{\mathrm{T}} \cdot \overrightarrow{\dot{u}}_{\mathrm{N}} \tag{77}$$

Using Eq. (77), the integration of Eq. (22) in region V can be rewritten with vector form as

$$\int_V \frac{\gamma^{\mathrm{w}}}{nk^{\mathrm{w}}} \overrightarrow{B}_{\mathrm{v}}^{\mathrm{T}} \cdot \overrightarrow{\dot{u}}_{\mathrm{N}} \mathrm{d}V - \int_V \frac{\partial^2 p_{\mathrm{dE}}^{\mathrm{w}}}{\partial x_i \partial x_i} \mathrm{d}V - \int_V \frac{\gamma^{\mathrm{w}}}{k^{\mathrm{w}} K^{\mathrm{w}}} \dot{p}_{\mathrm{dE}}^{\mathrm{w}} \mathrm{d}V - \int_V \frac{3\gamma^{\mathrm{w}} \alpha_{\mathrm{T}}^{\mathrm{w}}}{k^{\mathrm{w}}} [N] \mathrm{d}V \dot{\theta}_{\mathrm{N}} + \int_V \frac{\gamma^{\mathrm{w}}}{k^{\mathrm{w}} S_{\mathrm{r}}} \dot{S}_{\mathrm{r}} \mathrm{d}V = 0 \tag{78}$$

Because the EPWP is assumed as constant within an element, Eq. (78) can be rewritten as

$$\int_V \frac{\gamma^{\mathrm{w}}}{nk^{\mathrm{w}}} \overrightarrow{B}_{\mathrm{v}}^{\mathrm{T}} \cdot \overrightarrow{\dot{u}}_{\mathrm{N}} \mathrm{d}V - \int_V \frac{\partial^2 p_{\mathrm{dE}}^{\mathrm{w}}}{\partial x_i \partial x_i} \mathrm{d}V - A\dot{p}_{\mathrm{dE}}^{\mathrm{w}} - [K_{\mathrm{WT}}]\dot{\theta}_{\mathrm{N}} + \int_V \frac{\gamma^{\mathrm{w}}}{k^{\mathrm{w}} S_{\mathrm{r}}} \dot{S}_{\mathrm{r}} \mathrm{d}V = 0 \tag{79}$$

$$\left.\begin{aligned} A &= \int_V \frac{\gamma^{\mathrm{w}}}{k^{\mathrm{w}} K^{\mathrm{w}}} \mathrm{d}V = \frac{\gamma^{\mathrm{w}}}{k^{\mathrm{w}} K^{\mathrm{w}}} \overline{V} \\ [K_{\mathrm{WT}}] &= \int_V \frac{3\gamma^{\mathrm{w}} \alpha_{\mathrm{T}}^{\mathrm{w}}}{k^{\mathrm{w}}} [N] \mathrm{d}V \end{aligned}\right\} \tag{80}$$

where $\overline{V}$ is the volume of region V. The volume integration of the second term on left side of Eq. (79) can be calculated as follows:

$$\left.\begin{aligned} \int_V \frac{\partial^2 p_{\mathrm{dE}}^{\mathrm{w}}}{\partial x_i \partial x_i} \mathrm{d}V &= \alpha p_{\mathrm{dE}}^{\mathrm{w}} - \sum_{i=1}^{m} \alpha_i p_{i|\mathrm{dE}}^{\mathrm{w}} \\ \alpha &= \sum_{i=1}^{m} \frac{A_i}{s_i} \\ \alpha_i &= \frac{A_i}{s_i} \end{aligned}\right\} \tag{81}$$

where m is the number of element sides (e.g. $m = 4$ for four-node element of two dimensions) or element faces (e.g. $m = 6$ for hexahedron element of three dimensions), S_i is the center-to-center distance of an arbitrary element to its ith neighboring element, b_i is the drainage area of an arbitrary element in edge i.

Because of static problem, the change of soil displacement, PWP and degree of saturation can be calculated by finite difference method:

$$\left.\begin{aligned} \overrightarrow{\dot{u}}_{\mathrm{N}} &= \frac{\Delta \overrightarrow{u}_{\mathrm{N}|t+\Delta t}}{\Delta t} = \frac{\overrightarrow{u}_{\mathrm{N}|t+\Delta t} - \overrightarrow{u}_{\mathrm{N}|t}}{\Delta t} \\ \dot{p}_{\mathrm{dE}}^{\mathrm{w}} &= \frac{\Delta p_{\mathrm{dE}|t+\Delta t}^{\mathrm{w}}}{\Delta t} = \frac{p_{\mathrm{dE}|t+\Delta t}^{\mathrm{w}} - p_{\mathrm{dE}|t}^{\mathrm{w}}}{\Delta t} \end{aligned}\right\} \tag{82}$$

$$\left.\begin{aligned} \dot{p}_{\mathrm{dE}}^{\mathrm{a}} &= \frac{\Delta p_{\mathrm{dE}|t+\Delta t}^{\mathrm{a}}}{\Delta t} = \frac{p_{\mathrm{dE}|t+\Delta t}^{\mathrm{a}} - p_{\mathrm{dE}|t}^{\mathrm{a}}}{\Delta t} \\ \dot{S}_{\mathrm{r}} &= \frac{\Delta S_{\mathrm{r}|t+\Delta t}}{\Delta t} = \frac{S_{\mathrm{r}|t+\Delta t} - S_{\mathrm{r}|t}}{\Delta t} \end{aligned}\right\} \tag{83}$$

$$\dot{\theta}_{\mathrm{N}} = \frac{\Delta \theta_{\mathrm{N}|t+\Delta t}}{\Delta t} = \frac{\theta_{\mathrm{N}|t+\Delta t} - \theta_{\mathrm{N}|t}}{\Delta t} \tag{84}$$

Substituting Eqs. (71), (72), (77), (80)–(84) into Eq. (79), the following equation can be obtained:

$$\begin{aligned} &S_{\mathrm{r}|t} \overrightarrow{K}_{\mathrm{v}}^{\mathrm{T}} \Delta \overrightarrow{u}_{\mathrm{N}|t+\Delta t} - \frac{k^{\mathrm{w}} \Delta t}{\gamma^{\mathrm{w}}} n S_{\mathrm{r}|t} \alpha p_{\mathrm{dE}|t+\Delta t}^{\mathrm{w}} + \frac{k^{\mathrm{w}}}{\gamma^{\mathrm{w}}} \left(n S_{\mathrm{r}|t} A + \frac{\gamma^{\mathrm{w}}}{k^{\mathrm{w}}} n \overline{V} \boldsymbol{k}_{\mathrm{s}}^{-1} \right) \\ &\quad \times p_{\mathrm{dE}|t+\Delta t}^{\mathrm{w}} + n \overline{V} \boldsymbol{k}_{\mathrm{s}}^{-1} p_{\mathrm{dE}|t+\Delta t}^{\mathrm{a}} + \sum_{i=1}^{m} \frac{k^{\mathrm{w}} \Delta t}{\gamma^{\mathrm{w}}} n \alpha_i S_{\mathrm{r}|t} p_{\mathrm{idE}|t+\Delta t}^{\mathrm{w}} \\ &\quad = \frac{k^{\mathrm{w}}}{\gamma^{\mathrm{w}}} \left(A n S_{\mathrm{r}|t} - \frac{\gamma^{\mathrm{w}}}{k^{\mathrm{w}}} n \overline{V} \boldsymbol{k}_{\mathrm{s}}^{-1} \right) p_{\mathrm{dE}|t}^{\mathrm{w}} + n \overline{V} \boldsymbol{k}_{\mathrm{s}}^{-1} p_{\mathrm{dE}|t}^{\mathrm{a}} \\ &\quad + [K_{\mathrm{WT}}] \Delta \theta_{\mathrm{N}|t+\Delta t} \end{aligned} \tag{85}$$

By defining the following equations:

$$\left.\begin{aligned} \overline{\alpha} &= \frac{n S_{\mathrm{r}|t} \Delta t k^{\mathrm{w}}}{\gamma^{\mathrm{w}}} \alpha, \ \overline{\alpha}_i = \frac{n S_{\mathrm{r}|t} \Delta t k^{\mathrm{w}}}{\gamma^{\mathrm{w}}} \alpha_i \\ \overline{A} &= \frac{n S_{\mathrm{r}|t} k^{\mathrm{w}}}{\gamma^{\mathrm{w}}} A, \ F_{\mathrm{sr}} = n \overline{V} \boldsymbol{k}_{\mathrm{s}}^{-1} \end{aligned}\right\} \tag{86}$$

$$\left[\overline{K}_{\mathrm{WT}}\right] = \frac{n S_{\mathrm{r}} k^{\mathrm{w}}}{\gamma^{\mathrm{w}}} [K_{\mathrm{WT}}] = 3 n S_{\mathrm{r}} \alpha_{\mathrm{T}}^{\mathrm{w}} \int_V [N] \mathrm{d}V \tag{87}$$

and substituting Eqs. (86) and (87) into Eq. (79), the discretization of continuum equation of liquid phase in space and time can be written as

$$\begin{aligned} &S_{\mathrm{r}|t} \overrightarrow{K}_{\mathrm{v}}^{\mathrm{T}} \Delta \overrightarrow{u}_{\mathrm{N}|t+\Delta t} - \left(\overline{\alpha} + \overline{A} + F_{\mathrm{sr}} \right) p_{\mathrm{dE}|t+\Delta t}^{\mathrm{w}} + F_{\mathrm{sr}} p_{\mathrm{dE}|t+\Delta t}^{\mathrm{a}} \\ &\quad + \sum_{i=1}^{m} \overline{\alpha}_i p_{\mathrm{idE}|t+\Delta t}^{\mathrm{w}} = -\left(\overline{A} + F_{\mathrm{sr}} \right) p_{\mathrm{dE}|t}^{\mathrm{w}} + F_{\mathrm{sr}} p_{\mathrm{dE}|t}^{\mathrm{a}} \\ &\quad + \left[\overline{K}_{\mathrm{WT}} \right] \Delta \theta_{\mathrm{N}|t+\Delta t} \end{aligned} \tag{88}$$

2.7. Discretization of continuum equation of air phase in space and time

The discretization of continuum equation of air phase can be implemented by the same way as liquid phase. Integration of Eq. (28) in region V with the vector form can be written as

$$\int_V \frac{\gamma^{\mathrm{a}}}{nk^{\mathrm{a}}} \overrightarrow{B}_{\mathrm{v}}^{\mathrm{T}} \overrightarrow{\dot{u}}_{\mathrm{N}} \mathrm{d}V - \int_V \frac{\partial^2 p_{\mathrm{dE}}^{\mathrm{a}}}{\partial x_i \partial x_i} \mathrm{d}V - \int_V \frac{\gamma^{\mathrm{a}}}{k^{\mathrm{a}} K^{\mathrm{a}}} \dot{p}_{\mathrm{dE}}^{\mathrm{a}} \mathrm{d}V - \int_V \frac{3\gamma^{\mathrm{a}} \alpha_{\mathrm{T}}^{\mathrm{a}}}{k^{\mathrm{a}}} [N] \mathrm{d}V \dot{\theta}_{\mathrm{N}} - \int_V \frac{\gamma^{\mathrm{a}}}{k^{\mathrm{a}} (1 - S_{\mathrm{r}})} \dot{S}_{\mathrm{r}} \mathrm{d}V = 0 \tag{89}$$

Because the PAP is also assumed to be constant within an element, Eq. (89) can be rewritten as

$$\int_V \frac{\gamma^{\mathrm{a}}}{nk^{\mathrm{a}}} \overrightarrow{B}_{\mathrm{v}}^{\mathrm{T}} \overrightarrow{\dot{u}}_{\mathrm{N}} \mathrm{d}V - \int_V \frac{\partial^2 p_{\mathrm{dE}}^{\mathrm{a}}}{\partial x_i \partial x_i} \mathrm{d}V - B\dot{p}_{\mathrm{dE}}^{\mathrm{a}} - [K_{\mathrm{AT}}]\dot{\theta}_{\mathrm{N}} - \int_V \frac{\gamma^{\mathrm{a}}}{k^{\mathrm{a}} (1 - S_{\mathrm{r}})} \dot{S}_{\mathrm{r}} \mathrm{d}V = 0 \tag{90}$$

where

$$\left.\begin{aligned} B &= \int_V \frac{\gamma^{\mathrm{a}}}{k^{\mathrm{a}}K^{\mathrm{a}}}\mathrm{d}V = \frac{\gamma^{\mathrm{a}}}{k^{\mathrm{a}}K^{\mathrm{a}}}\overline{V} \\ [K_{\mathrm{AT}}] &= \int_V \frac{3\gamma^{\mathrm{a}}\alpha_{\mathrm{T}}^{\mathrm{a}}}{k^{\mathrm{a}}}[N]\mathrm{d}V \end{aligned}\right\} \tag{91}$$

The volume integration of the second term on left side of Eq. (90) can also be calculated by the same way as liquid phase:

$$\int_V \frac{\partial^2 p_{\mathrm{dE}}^{\mathrm{a}}}{\partial x_i \partial x_i}\mathrm{d}V = \alpha p_{\mathrm{dE}}^{\mathrm{a}} - \sum_{i=1}^{m}\alpha_i p_{i|\mathrm{dE}}^{\mathrm{a}} \tag{92}$$

Substituting Eqs. (71), (72), (77), (82)–(84) and (91), (92) into Eq. (90), the following equation can be obtained:

$$\begin{aligned} &\left(1-S_{\mathrm{r}|t}\right)\vec{K}_{\mathrm{v}}^{\mathrm{T}}\cdot\Delta\vec{u}_{\mathrm{N}|t+\Delta t} + n\overline{V}\boldsymbol{k}_{\mathrm{s}}^{-1}p_{\mathrm{dE}|t+\Delta t}^{\mathrm{w}} \\ &+\sum_{i=1}^{m}\frac{k^{\mathrm{a}}\Delta t}{\gamma^{\mathrm{a}}}n\alpha_i\left(1-S_{\mathrm{r}|t}\right)p_{i\mathrm{dE}|t+\Delta t}^{\mathrm{a}} - \frac{k^{\mathrm{a}}\cdot\Delta t}{\gamma^{\mathrm{a}}}n\left(1-S_{\mathrm{r}|t}\right)\alpha p_{\mathrm{dE}|t+\Delta t}^{\mathrm{a}} \\ &+\frac{k^{\mathrm{a}}}{\gamma^{\mathrm{a}}}\left[n\left(1-S_{\mathrm{r}|t}\right)B + \frac{\gamma^{\mathrm{a}}}{k^{\mathrm{a}}}n\overline{V}\boldsymbol{k}_{\mathrm{s}}^{-1}\right]p_{\mathrm{dE}|t+\Delta t}^{\mathrm{a}} \\ &= -\frac{k^{\mathrm{a}}}{\gamma^{\mathrm{a}}}\left[n\left(1-S_{\mathrm{r}|t}\right)B + \frac{\gamma^{\mathrm{a}}}{k^{\mathrm{a}}}n\overline{V}\boldsymbol{k}_{\mathrm{s}}^{-1}\right]p_{\mathrm{dE}|t}^{\mathrm{a}} + n\overline{V}\boldsymbol{k}_{\mathrm{s}}^{-1}p_{\mathrm{dE}|t}^{\mathrm{w}} \\ &+\frac{nk^{\mathrm{a}}}{\gamma^{\mathrm{a}}}[K_{\mathrm{AT}}]\Delta\theta_{\mathrm{N}|t+\Delta t} \end{aligned} \tag{93}$$

By defining the following equations:

$$\left.\begin{aligned} \overline{\beta} &= \frac{n\left(1-S_{\mathrm{r}|t}\right)\Delta t k^{\mathrm{a}}}{\gamma^{\mathrm{a}}}\alpha,\ \overline{\beta}_i = \frac{n\left(1-S_{\mathrm{r}|t}\right)\Delta t k^{\mathrm{a}}}{\gamma^{\mathrm{a}}}\alpha_i \\ \overline{B} &= \frac{n\left(1-S_{\mathrm{r}|t}\right)k^{\mathrm{a}}}{\gamma^{\mathrm{a}}}B \end{aligned}\right\} \tag{94}$$

$$\left[\overline{K}_{\mathrm{AT}}\right] = \frac{n(1-S_{\mathrm{r}})k^{\mathrm{a}}}{\gamma^{\mathrm{a}}}[K_{\mathrm{AT}}] = 3n(1-S_{\mathrm{r}})\alpha_{\mathrm{T}}^{\mathrm{a}}\int_V [N]\mathrm{d}V \tag{95}$$

and substituting Eqs. (94) and (95) into Eq. (93), the discretization of continuum equation of air phase in space and time can be written as

$$\begin{aligned} &\left(1-S_{\mathrm{r}|t}\right)\vec{K}_{\mathrm{v}}^{\mathrm{T}}\Delta\vec{u}_{\mathrm{N}|t+\Delta t} + F_{\mathrm{sr}}p_{\mathrm{dE}|t+\Delta t}^{\mathrm{w}} - \left(\overline{\beta}+\overline{B}+F_{\mathrm{sr}}\right)p_{\mathrm{dE}|t+\Delta t}^{\mathrm{a}} \\ &\quad+\sum_{i=1}^{m}\overline{\beta}_i p_{i\mathrm{dE}|t+\Delta t}^{\mathrm{a}} = F_{\mathrm{sr}}p_{\mathrm{dE}|t}^{\mathrm{w}} - (\overline{B}+F_{\mathrm{sr}})p_{\mathrm{dE}|t}^{\mathrm{a}} \\ &\quad+\left[\overline{K}_{\mathrm{AT}}\right]\Delta\theta_{\mathrm{N}|t+\Delta t} \end{aligned} \tag{96}$$

2.8. Discretization of energy conservation equation of air phase in space and time

Based on the Galerkin method, the energy conservation equation can be discretized in space for adopting into the FEM.

At any arbitrary time t, the temperature $\theta(x,y,z,t)$ of any arbitrary point within any arbitrary element can be expressed by the nodal temperatures of this element. So, the temperature can be written as

$$\boldsymbol{\theta} = [N]\boldsymbol{\theta}_{\mathrm{N}} \tag{97}$$

where $[N]$ is the shape function matrix, and $\boldsymbol{\theta}_{\mathrm{N}}$ is the matrix of nodal temperatures at an arbitrary time within an element. Using the Galerkin method, the energy conservation Eq. (34) in any arbitrary element can be expressed as

$$\begin{aligned} &\int_V [N]^{\mathrm{T}}\left(\overline{k}_{\mathrm{t}}\frac{\partial^2\boldsymbol{\theta}}{\partial x_i\partial x_i} + E - \overline{\rho c}\frac{\partial\boldsymbol{\theta}}{\partial t}\right)\mathrm{d}V - \int_V [N]^{\mathrm{T}}\left[nS_{\mathrm{r}}(\rho c)^{\mathrm{w}}v_i^{\mathrm{w}}\frac{\partial\boldsymbol{\theta}}{\partial x_i}\right. \\ &\left.+\,n(1-S_{\mathrm{r}})(\rho c)^{\mathrm{a}}v_i^{\mathrm{a}}\frac{\partial\boldsymbol{\theta}}{\partial x_i}\right]\mathrm{d}V = 0 \end{aligned} \tag{98}$$

Based on the Green–Gauss theorem, we have

$$\int_V \overline{k}_{\mathrm{t}}[N]^{\mathrm{T}}\frac{\partial^2\boldsymbol{\theta}}{\partial x_i\partial x_i}\mathrm{d}V = -\int_V \overline{k}_{\mathrm{t}}\frac{\partial[N]^{\mathrm{T}}}{\partial x_i}\frac{\partial\boldsymbol{\theta}}{\partial x_i}\mathrm{d}V + \int_S \overline{k}_{\mathrm{t}}[N]^{\mathrm{T}}\frac{\partial\boldsymbol{\theta}}{\partial n}\mathrm{d}S \tag{99}$$

where $\partial/\partial n$ is the partial differentiation of the surface's outward normal direction.

With Fourier's law and substituting Eq. (97) into the right side of Eq. (99), it can be rewritten as

$$\begin{aligned} &-\int_V \overline{k}_{\mathrm{t}}\frac{\partial[N]^{\mathrm{T}}}{\partial x_i}\frac{\partial\boldsymbol{\theta}}{\partial x_i}\mathrm{d}V + \int_S \overline{k}_{\mathrm{t}}[N]^{\mathrm{T}}\frac{\partial\boldsymbol{\theta}}{\partial n}\mathrm{d}S \\ &\quad= -\int_V \overline{k}_{\mathrm{t}}\frac{\partial[N]^{\mathrm{T}}}{\partial x_i}\frac{\partial[N]}{\partial x_i}\mathrm{d}V\boldsymbol{\theta}_{\mathrm{N}} - \int_S q[N]^{\mathrm{T}}\mathrm{d}S \end{aligned} \tag{100}$$

Then, by substituting Eqs. (97) and (100) into Eq. (98), we have

$$\begin{aligned} &\int_V \overline{k}_{\mathrm{t}}\frac{\partial[N]^{\mathrm{T}}}{\partial x_i}\frac{\partial[N]}{\partial x_i}\mathrm{d}V\boldsymbol{\theta}_{\mathrm{N}} + \int_S q[N]^{\mathrm{T}}\mathrm{d}S - \int_V [N]^{\mathrm{T}}E\mathrm{d}V \\ &\quad+\int_V \overline{\rho c}[N]^{\mathrm{T}}[N]\mathrm{d}V\dot{\boldsymbol{\theta}}_{\mathrm{N}} + \int_V nS_{\mathrm{r}}(\rho c)^{\mathrm{w}}v_i^{\mathrm{w}}[N]^{\mathrm{T}}\frac{\partial[N]}{\partial x_i}\mathrm{d}V\boldsymbol{\theta}_{\mathrm{N}} \\ &\quad+\int_V n(1-S_{\mathrm{r}})(\rho c)^{\mathrm{a}}v_i^{\mathrm{a}}[N]^{\mathrm{T}}\frac{\partial[N]^{\mathrm{T}}}{\partial x_i}\mathrm{d}V\boldsymbol{\theta}_{\mathrm{N}} = 0 \end{aligned} \tag{101}$$

The equations can be defined as follows:

$$[C^{\mathrm{t}}] = \int_V \overline{\rho c}[N][N]\mathrm{d}V \tag{102}$$

$$\begin{aligned} [K^{\mathrm{t}}] &= \int_V \overline{k}_{\mathrm{t}}\frac{\partial[N]^{\mathrm{T}}}{\partial x_i}\frac{\partial[N]}{\partial x_i}\mathrm{d}V + \int_V nS_{\mathrm{r}}(\rho c)^{\mathrm{w}}v_i^{\mathrm{w}}[N]^{\mathrm{T}}\frac{\partial[N]}{\partial x_i}\mathrm{d}V \\ &\quad+\int_V n(1-S_{\mathrm{r}})(\rho c)^{\mathrm{a}}v_i^{\mathrm{a}}[N]^{\mathrm{T}}\frac{\partial[N]}{\partial x_i}\mathrm{d}V \end{aligned} \tag{103}$$

$$[f^{\mathrm{t}}] = \int_V [N]^{\mathrm{T}}E\mathrm{d}V - \int_S q[N]^{\mathrm{T}}\mathrm{d}S \tag{104}$$

Therefore, Eq. (101) can be rewritten as

$$[C^{\mathrm{t}}]\dot{\boldsymbol{\theta}}_{\mathrm{N}} + [K^{\mathrm{t}}]\boldsymbol{\theta}_{\mathrm{N}} = [f^{\mathrm{t}}] \tag{105}$$

In this section, the Newmark method will be used for discretization of the energy conservation equation in time. The current time is denoted as $t + \Delta t$ in derivation, Eq. (105) can be written as

$$[C^{t}]\dot{\boldsymbol{\theta}}_{N|t+\Delta t} + [K^{t}]\boldsymbol{\theta}_{N|t+\Delta t} = [f^{t}] \tag{106}$$

According to the Newmark method and the intermediate value theorem, the temperature of current time can be expressed as

$$\boldsymbol{\theta}_{N|t+\Delta t} = \boldsymbol{\theta}_{N|t} + \Delta t\dot{\boldsymbol{\theta}}_{N|t} + \beta\Delta t\left(\dot{\boldsymbol{\theta}}_{N|t+\Delta t} - \dot{\boldsymbol{\theta}}_{N|t}\right) \tag{107}$$

where β is a parameter with a value $0 \le \beta \le 1$. When the parameter β is equal to or greater than 0.5, iteration calculation will always be convergent.

By substituting Eq. (107) into Eq. (106), the energy conservation discretized in space and time can be obtained:

$$\left([C^{t}] + \beta\Delta t[K^{t}]\right)\dot{\boldsymbol{\theta}}_{N|t+\Delta t} = [f^{t}] - [K^{t}]\left[\boldsymbol{\theta}_{N|t} + (1-\beta)\Delta t\dot{\boldsymbol{\theta}}_{N|t}\right] \tag{108}$$

Combining Eqs. (73), (88), (96) and (108), THMA FE-FD formulation for static analysis can be obtained:

$$\begin{bmatrix} [K] & \overrightarrow{I}^{w}_{Sat} & \overrightarrow{I}^{a}_{Sat} \\ S_r\overrightarrow{K}^{T}_{v} & -\left[\overline{\alpha}+\overline{A}+F_{sr}\right] & F_{sr} \\ (1-S_r)\overrightarrow{K}^{T}_{v} & F_{sr} & -\left[\overline{\beta}+\overline{B}+F_{sr}\right] \end{bmatrix} \begin{Bmatrix} \Delta\overrightarrow{u}_{N|t+\Delta t} \\ p^{w}_{dE|t+\Delta t} \\ p^{a}_{dE|t+\Delta t} \end{Bmatrix} + \begin{Bmatrix} 0 \\ \sum_{i=1}^{m}\overline{\alpha}_i p^{w}_{idE|t+\Delta t} \\ \sum_{i=1}^{m}\overline{\beta}_i p^{a}_{idE|t+\Delta t} \end{Bmatrix} = \begin{bmatrix} \Delta\overrightarrow{F}_{|t+\Delta t} + \overrightarrow{F}_T\Delta\theta_{N|t+\Delta t} + \overrightarrow{I}^{w}_{Sat}p^{w}_{dE|t} + \overrightarrow{I}^{a}_{Sat}p^{a}_{dE|t} \\ -\left(\overline{A}+F_{sr}\right)p^{w}_{dE|t} + F_{sr}p^{a}_{dE|t} + \left[\overline{K}_{WT}\right]\Delta\theta_{N|t+\Delta t} \\ F_{sr}p^{w}_{dE|t} - (\overline{B}+F_{sr})p^{a}_{dE|t} + \left[\overline{K}_{AT}\right]\Delta\theta_{N|t+\Delta t} \end{bmatrix} \tag{109}$$

$$\left([C^{t}] + \beta\Delta t[K^{t}]\right)\dot{\boldsymbol{\theta}}_{N|t+\Delta t} = [f^{t}] - [K^{t}]\left[\boldsymbol{\theta}_{N|t} + (1-\beta)\Delta t\dot{\boldsymbol{\theta}}_{N|t}\right] \tag{110}$$

Because the total water head is conveniently used as the unknown in the FEM program, from the relation, $p^{w}_{d} = \gamma^{w}h^{w}_{d}$ ($h^{w} = h^{w}_{d} + h^{w}_{ini}$, $p^{w} = p^{w}_{d} + p^{w}_{ini}$), the THMA coupling FEM equation can be rewritten as

$$\begin{bmatrix} [K] & \gamma^{w}\overrightarrow{H}^{w}_{Sat} & \overrightarrow{H}^{a}_{Sat} \\ S_r\overrightarrow{K}^{T}_{v} & -\gamma^{w}\left[\overline{\alpha}+\overline{A}+F_{sr}\right] & F_{sr} \\ (1-S_r)\overrightarrow{K}^{T}_{v} & \gamma^{w}F_{sr} & -\left[\overline{\beta}+\overline{B}+F_{sr}\right] \end{bmatrix} \times \begin{Bmatrix} \Delta\overrightarrow{u}_{N|t+\Delta t} \\ h^{w}_{dE|t+\Delta t} \\ p^{a}_{dE|t+\Delta t} \end{Bmatrix} + \begin{Bmatrix} 0 \\ \sum_{i=1}^{m}\overline{\alpha}_i\gamma^{w}h^{w}_{idE|t+\Delta t} \\ \sum_{i=1}^{m}\overline{\beta}_i p^{a}_{idE|t+\Delta t} \end{Bmatrix} = \begin{bmatrix} \Delta\overrightarrow{F}_{|t+\Delta t} + \overrightarrow{F}_T\Delta\theta_{N|t+\Delta t} + \gamma^{w}\overrightarrow{H}^{w}_{Sat}h^{w}_{dE|t} + \overrightarrow{H}^{a}_{Sat}p^{a}_{dE|t} \\ -\left(\overline{A}+F_{sr}\right)\gamma^{w}h^{w}_{dE|t} + F_{sr}p^{a}_{dE|t} + \left[\overline{K}_{WT}\right]\Delta\theta_{N|t+\Delta t} \\ F_{sr}\gamma^{w}h^{w}_{dE|t} - (\overline{B}+F_{sr})p^{a}_{dE|t} + \left[\overline{K}_{AT}\right]\Delta\theta_{N|t+\Delta t} \end{bmatrix} \tag{111}$$

$$\left([C^{t}] + \beta\Delta t[K^{t}]\right)\dot{\boldsymbol{\theta}}_{N|t+\Delta t} = [f^{t}] - [K^{t}]\left[\boldsymbol{\theta}_{N|t} + (1-\beta)\Delta t\dot{\boldsymbol{\theta}}_{N|t}\right] \tag{112}$$

where

$$\overrightarrow{H}^{w}_{Sat} = \overrightarrow{K}_v S_{r|t} - \left(\overrightarrow{K}_v\gamma^{w}h^{w}_{dE|t} - \overrightarrow{K}_v p^{a}_{dE|t} - \overrightarrow{K}_{Sat}\right)\boldsymbol{k}_s^{-1} \tag{113}$$

$$\overrightarrow{H}^{a}_{Sat} = \left(1-S_{r|t}\right)\overrightarrow{K}_v + \left(\overrightarrow{K}_v\gamma^{w}h^{w}_{dE|t} - \overrightarrow{K}_v p^{a}_{dE|t} - \overrightarrow{K}_{Sat}\right)\boldsymbol{k}_s^{-1} \tag{114}$$

3. Thermo-hydro-mechanical-air coupling analysis of a heating test in unsaturated ground

3.1. Brief description of heating experiment

The heating experiment is a large-scale heating test carried out in the Mont Terri Underground Rock Laboratory (Munoz, 2006). The objective of the heating experiment is to understand the behavior of the host rock and the bentonite buffer (artificial barrier) within the THM coupling processes. The heating test site is located on the so-called "HE niche" on the west wall of the New Gallery of the underground rock laboratory, in the shaly facies of the Opalinus clay formations. Fig. 1 shows the bird view of the Mont Terri Underground Rock Laboratory and the location of the HE niche. A vertical borehole 0.30 m in diameter and 7.0 m in depth, identified as BHE-0, was drilled in the niche floor as shown in Fig. 2. A heating

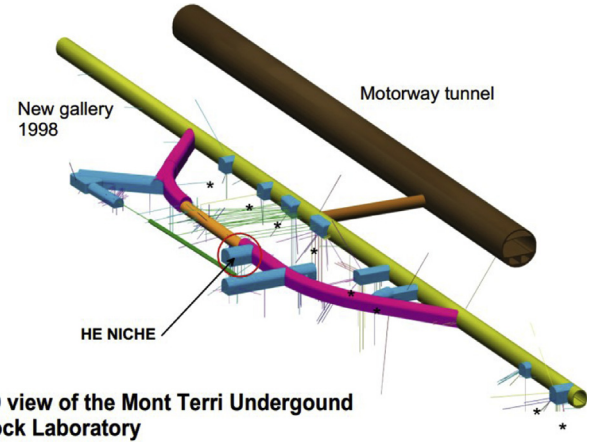

Fig. 1. Bird view of Mont Terri Underground Rock Laboratory and location of HE niche (Munoz, 2006).

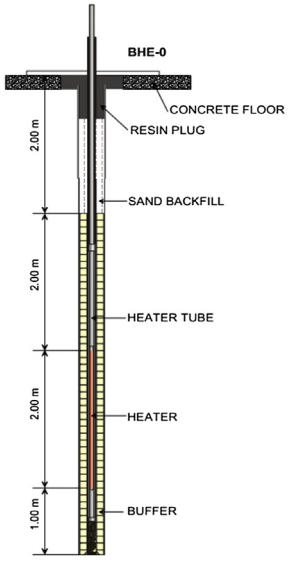

Fig. 2. Vertical section of borehole BHE-0 (Munoz, 2006).

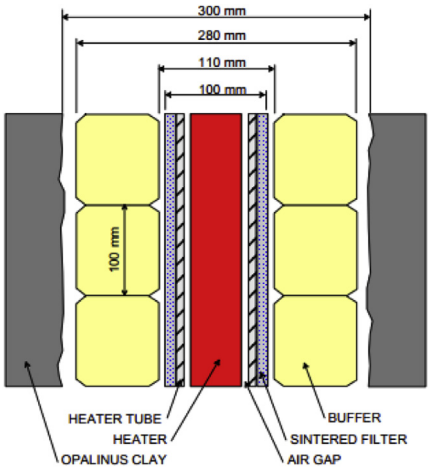

Fig. 3. Setup of heating test (Munoz, 2006).

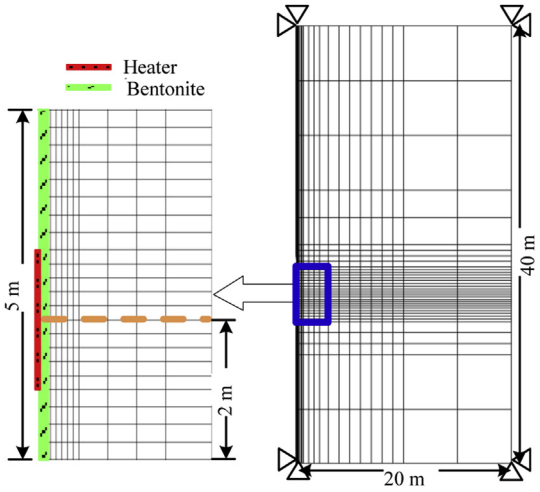

Fig. 4. 2D FEM mesh and mechanical boundary condition.

tube with an external diameter of 100 mm was placed in the axis of the borehole BHE-0. A heater of 75 mm in diameter and 2.0 m in length was placed into the heating tube, and the details of the test setup are shown in Fig. 3.

The heating experiment was conducted in 3 different phases. The first phase consists of the hydration of the bentonite buffer, which lasted for 982 days. The hydration of the bentonite buffer was performed at four different depths at piezometric head of 2.0 m over the niche floor and the surrounding natural rock. The second phase is heating phase once the bentonite buffer was fully saturated. Firstly, heat power was applied in steps of 140 W, 150 W,

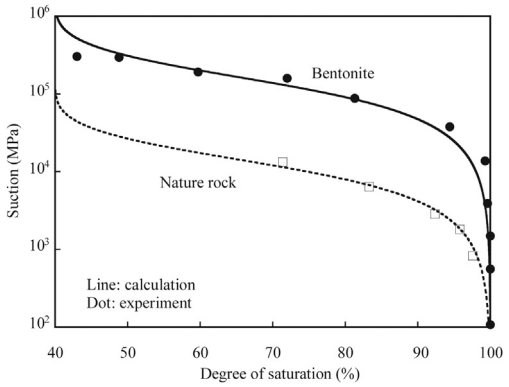

Fig. 5. Moisture characteristic curves of bentonite and host rock.

285 W and 580 W, until the heat-buffer contact reached a temperature of 100 °C. Then, a constant temperature of 100 °C was maintained at the heater-bentonite contact, with a heating period of 540 days. Finally the heat power was switched off and the cooling phase began. In the experiment, the PWP and the temperature at some selected points are measured.

3.2. Numerical simulation and results

Due to the symmetry condition, only half of the area is considered. Fig. 4 shows the two-dimensional (2D) FEM meshes and the mechanical boundary condition. In the analysis, the calculated results of THMA variables at some positions, marked with orange line in Fig. 4, are selected to compare with the test results. For simplicity, the materials are assumed to be homogeneous and isotropic, focusing on THMA coupling process in the rock-buffer system. An isotropic stress state with a magnitude of 5 MPa is assumed in the simulation. A total water head of 40 m is given for the host rock, and the initial temperature is 15 °C, being the same as the test conditions. In the simulation, the air pressure is assumed to be constant (i.e. the atmospheric pressure), the same condition as the test. Material parameters of the bentonite and the rock used in the simulation are listed in Table 1.

Fig. 5 shows the MCCs of the bentonite and the host rock used in the simulation. It is found that the calculated MCCs of the bentonite and the host rock match with well the test results. The parameters of the MCC of the bentonite and the host rock are listed in Table 2. In the simulation, the initial degree of saturation of the bentonite buffer is 70%, which corresponds to a suction of $s = 136$ MPa measured at the field test.

It is well known that the water permeability is dependent on the degree of saturation, that is, the permeability increases along with the increase of the saturation. The water permeability, however, was not measured in the test. In the THMA analysis of the heating

Table 1
Material parameters of bentonite and rock.

Material	Compression index, λ	Swelling index, κ	Critical state parameter, M	Void ratio, N ($p' = 98$ kPa on N.C.L.)	Poisson's ratio, ν	Parameter of overconsolidation, a	Parameter of suction, b
Bentonite	0.0050	0.010	1.80	1.04	0.30	5.0	0.00
Rock	0.0020	0.0001	1.90	0.62	0.30	5.0	0.00

Material	Parameter of overconsolidation, β	Void ratio, N_r ($p' = 98$ kPa on N.C.L.S.)	Thermal expansion coefficient (K^{-1})	Thermal expansion coefficient of water (K^{-1})	Thermal conductivity (kJ m^{-1} K^{-1} min^{-1})	Specific heat (kJ Mg^{-1} K^{-1})	Specific heat of water (kJ Mg^{-1} K^{-1})
Bentonite	1.0	1.06	1.0×10^{-5}	2.1×10^{-4}	0.06	723	4184
Rock	1.0	0.65	3.0×10^{-6}		0.12	874	

Note: N.C.L. is the normally consolidated line in saturated state; N.C.L.S. is the normally consolidated line in unsaturated state.

Table 2
Parameters of MCC.

Material	Saturated degrees of saturation, S_r^s	Residual degrees of saturation, S_r^r	Parameter corresponding to drying AEV, S_d (kPa)	Parameter corresponding to wetting AEV, S_w (kPa)
Bentonite	1.00	0.40	11,000	800
Rock	1.00	0.40	21,000	1000
Material	Initial stiffness of scanning curve, k_{sp}^e(kPa)	Parameter of shape function, c_1	Parameter of shape function, c_2	Parameter of shape function, c_3
Bentonite	25,000	0.000001	0.000005	30.0
Rock	90,000	0.00003	0.00006	50.0

test (as an alternative), an interpolation method employing some values of the permeability at some specified saturations is used to simulate the change of the permeability with saturation. The relation between the water permeability and the degree of saturation used in the analysis is shown in Fig. 6 in order to fit the results of heating experiment.

Fig. 7 shows the time evolution of the degree of saturation at different positions with elapsed time. It is known from this figure that the required time to fully saturate the bentonite is approximately 400 days.

Fig. 8 shows the transitory process of the degree of saturation in the surrounding rocks at different positions with time, in which desaturation and re-saturation processes were clearly observed. It is found in Fig. 8 that the rock reaches the full saturation again after approximately 600 days of the hydration.

Fig. 9 shows the distribution of the degree of saturation at specified time during the hydration phase. It is found that the rock near the bentonite firstly changes from saturated state to unsaturated state, this is because the water cannot transport in time due to the low permeability of rock. Later the rock was re-saturated with the migration of pore water.

Fig. 10 shows the evolutions of temperatures at different positions away from the heater. It is known that the THMA analysis can

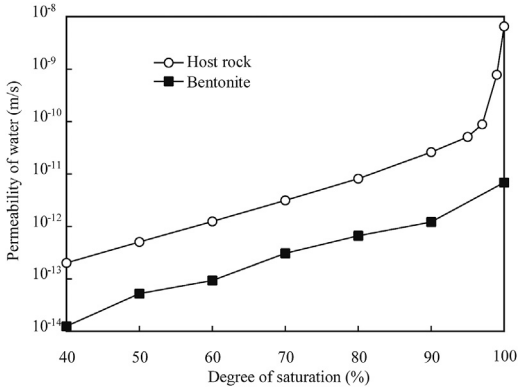

Fig. 6. Estimated relationships between water permeability and degree of saturation.

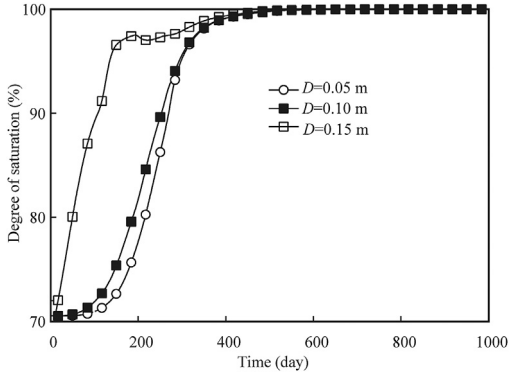

Fig. 7. Change of degree of saturation for bentonite during hydration phase. *D* is the distance away from the heater.

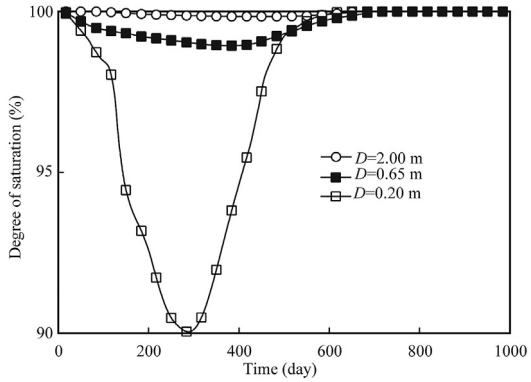

Fig. 8. Change of degree of saturation for rock during hydration phase.

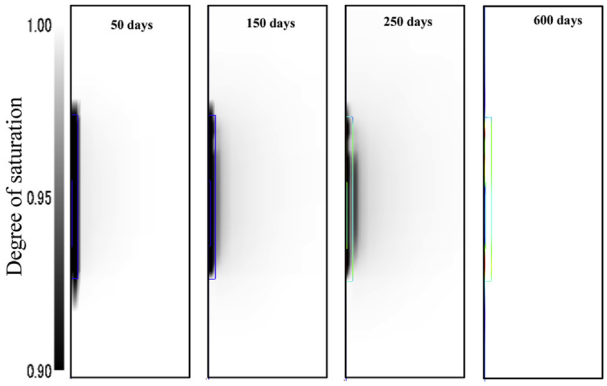

Fig. 9. Distribution of the degree of saturation at some specified times during hydration phase.

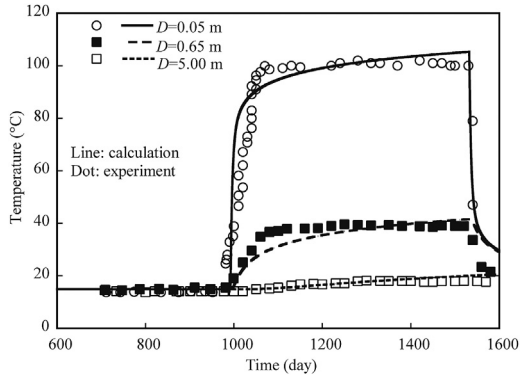

Fig. 10. Change of temperature with time at different positions in heating phase.

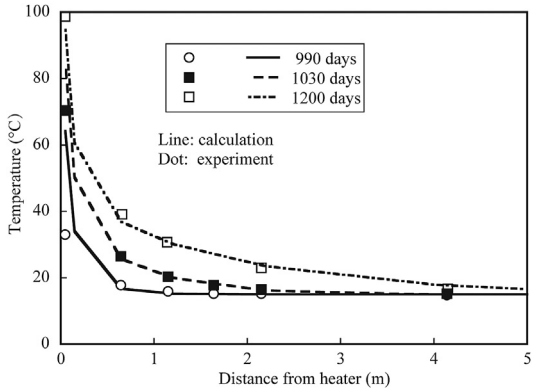

Fig. 11. Comparison of the temperature change obtained from the calculation and test at different positions.

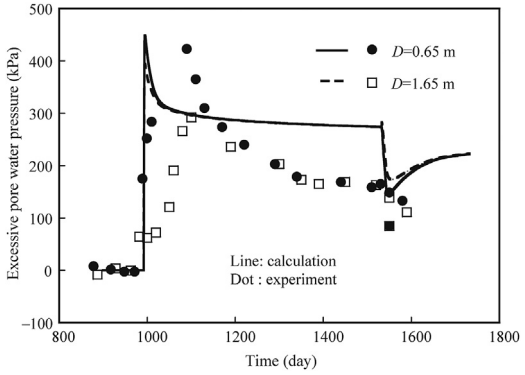

Fig. 12. Change of EPWP with time at different positions during heating and cooling phases.

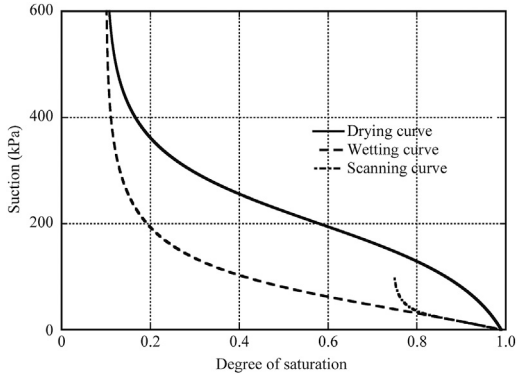

Fig. 13. MCC adopted for silty clay in simulation.

also well describe the change of temperatures measured in the HE-D experiment on the whole, such as the sharp increase and the sharp decrease of the temperature for all selected positions.

Fig. 11 shows the comparison of the temperature change obtained from the calculation and test at different positions. It is known from the figure that the nearer the distance from the heater is, the higher the temperature will be. There is no prominent increase of temperature at the distance 5 m away from the heater due to the low thermal conductivity of the rock.

Fig. 12 shows the change of EPWP with time at different positions during heating and cooling phases. It can be observed that the increase of temperature generates a significant increase of positive EPWP. The change of EPWP is mainly caused due to the fact that thermal expansion coefficient of water is much higher than that of the rock. Owing to the low permeability of rock, the drainage is slow and therefore the expansion of the pore water is impeded, resulting in an increase of the pore pressure at the initial time of heating. Later, as the migration of the pore water continues, EPWP is allowed to dissipate and consequentially turns to decrease. The simulation can well describe the test results on the whole.

4. Thermo-hydro-mechanical-air coupling simulation of model tests on slope failure in saturated/unsaturated Shirasu ground

4.1. Simulation of element tests

Triaxial tests on unsaturated silty clay under undrained and unvented conditions (Oka et al., 2010) are simulated by the proposed numerical method. The size of the test specimen is 50 mm in diameter and 100 mm in height. The initial cell pressure and air pressure were 450 kPa and 250 kPa, respectively. Four cases with different initial suctions, i.e. 10 kPa, 30 kPa, 50 kPa and 100 kPa, were considered and the strain-controlled loading rate is 0.005/min. In the simulation, the half size of the 3D specimen is considered because of the symmetric geometric and loading conditions in vertical direction. Fig. 13 shows the MCC for the silty clay in the simulation. The values of the parameters involved in the MCC are listed in Table 3. Because the tests were conducted in room temperature (20 °C) in the THMA analysis, the temperature, one of the state valuables, is also assigned as a constant throughout the simulation.

Fig. 14 shows the comparisons between the test and simulated results of the silty clay under fully undrained and unvented conditions. The left figures are the test results and the right ones are the simulations. The material parameters of the unsaturated silty clay are listed in Table 4. The way to calibrate the material parameters by triaxial tests can be referred to the work by Zhang and Ikariya (2011). From the test results, it is known that the higher the initial suction is, the larger the deviator stress at the same axial strain will be, and that the PWP and the PAP decrease with the increase of the initial suction. It is known by the comparisons that the simulation can describe the element tests in a satisfactory accuracy on the whole.

4.2. Simulation of model tests on slope failure in unsaturated Shirasu ground

Model tests (Kitamura et al., 2007) are also simulated to verify whether the proposed numerical method can describe the

Table 3
Parameters of MCC for silty clay.

Saturated degree of saturation, S_r^s	Residual degree of saturation, S_r^r	Parameter corresponding to drying AEV, S_d (kPa)	Parameter corresponding to wetting AEV, S_w (kPa)
0.99	0.10	220.2	5.10
Initial stiffness of scanning curve, k_{sp}^e (kPa)	Parameter of shape function, c_1	Parameter of shape function, c_2	Parameter of shape function, c_3
58,500	0.0108	0.010	24.0

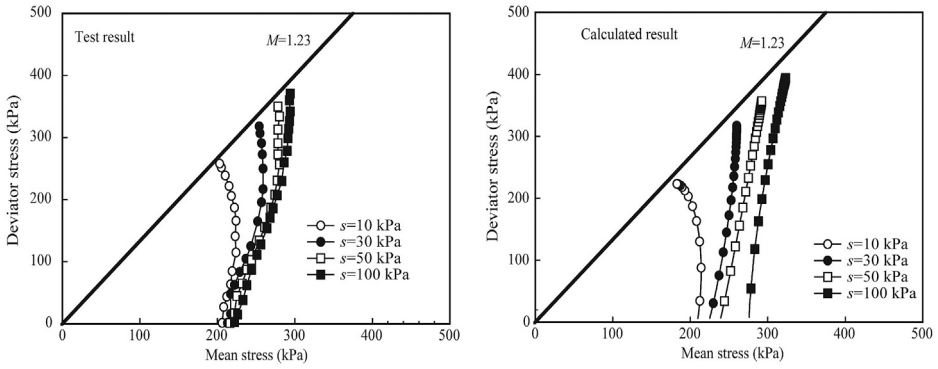

(a) Stress path.

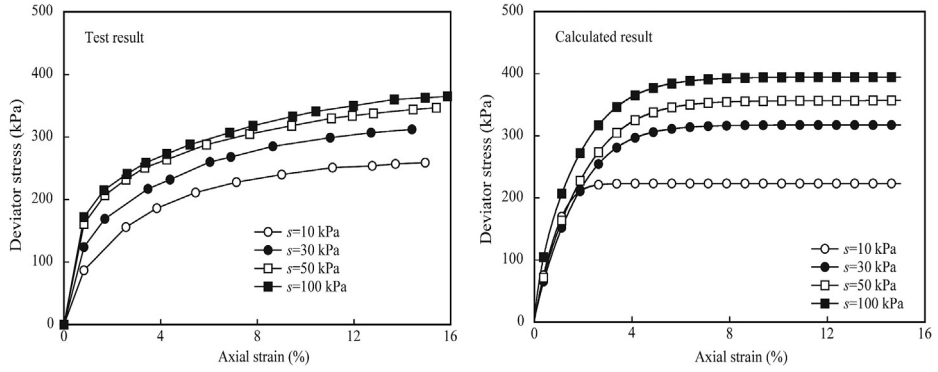

(b) Development of deviator stress.

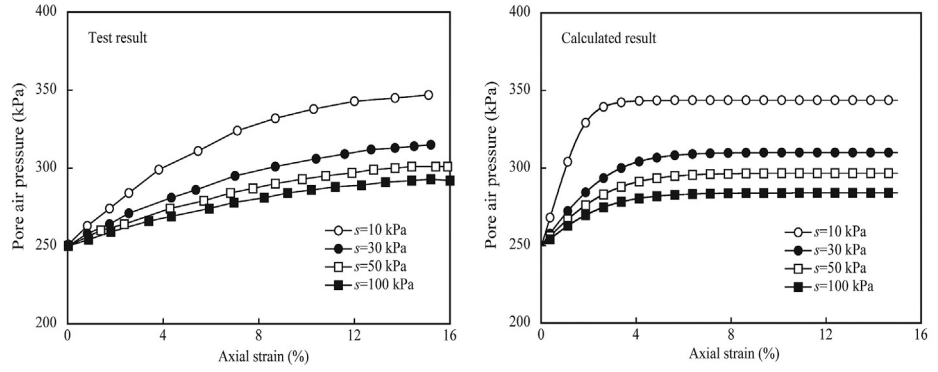

(c) Development of pore air pressure.

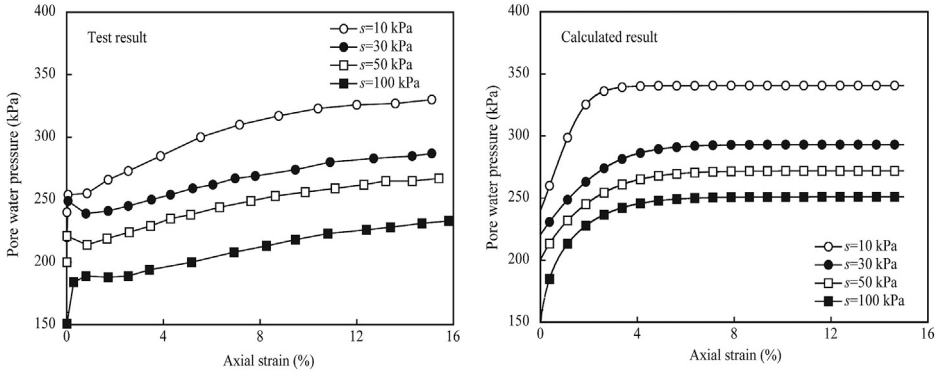

(d) Development of pore water pressure.

Fig. 14. Comparisons between the test and simulated results of silty clay under undrained and unvented conditions (test by Oka et al., 2010).

Table 4
Material parameters of silty clay.

Compression index, λ	Swelling index, κ	Critical state parameter, M	Void ratio, N ($p' = 98$ kPa on N.C.L.)	Poisson's ratio, ν
0.123	0.012	1.23	0.81	0.30
Parameter of overconsolidation, a	Parameter of suction, b	Parameter of overconsolidation, β	Void ratio, N_r ($p' = 98$ kPa on N.C.L.S.)	
5.00	0.50	1.00	1.12	

mechanism of slope failure in unsaturated Shirasu ground observed in the three different patterns of the model tests.

Fig. 15 shows the bird view of the test apparatus and the model ground (Kitamura et al., 2007). The ground of the model slope was made of a lightly compacted unsaturated Shirasu soil. The model slope was compacted carefully layer by layer (thickness of each layer is 5 cm). The physical properties of the soils are listed in Table 5 (Kitamura et al., 2007). The slope angle is 45° with a height of 80 cm. The permeable plates were used on the edges of the soil tank to control the drainage boundary condition.

Fig. 16 shows the layouts of measuring units, water injection positions and FEM mesh. In Case 3, an artificial turf sheet with holes was placed on the top surface of the slope in order to prevent water from washing away of the soils when water was showered from the ceiling with a manmade rainfall system. Fifteen tensiometers, indicated by No. 1 to No. 15, were buried in the model ground to measure the suction or the negative PWP.

Fig. 16b shows the finite element mesh used in the simulation of the slope failure. The size of FEM mesh, composed of 1681 nodes and 1600 4-node isoparametric elements, is the same as that of the model tests under plane strain condition. The boundary condition is given as: (a) for the displacement condition, it is fixed at the bottom in both x- and y-directions and is fixed at the vertical displacement in x-direction for only left surface. The other surfaces are free at x- and y-directions; (b) for drainage and vented conditions, the top and slope surfaces are permeable for all the cases, while the bottom and left surfaces are impermeable except for the range of water injection as shown in Fig. 16a.

The material parameters of the Shirasu soil used in the simulation are estimated based on the work by Kitamura et al. (1984) in which the mechanical properties of the Shirasu soil under the confining stress of 0.2–3.0 MPa were carefully investigated. The parameters listed in Table 6 are estimated based on the test results. Fig. 17 shows the theoretical stress–strain-dilatancy relations at constant confining stress but different constant suctions, under drained and vented conditions.

Because the initial negative PWPs measured in the tests are about −6 to −9 kPa in all three cases (Kitamura et al., 2007), for simplicity, the initial negative PWP in the simulation is assumed to be −8 kPa in the whole area for the three cases. The initial PAP is the atmospheric pressure and equal to 0 kPa both in the test and the simulation. The initial degree of saturation was measured at 38%, which is used also in the simulation. Fig. 18 shows the MCC of the Shirasu estimated from the test results (Kitamura et al., 2007). The parameters of the MCC are listed in Table 7.

As pointed out by Kamiya et al. (2006) that the permeability of air is dependent on the degree of saturation, based on the works by

Table 5
Physical properties and initial value of state variable ρ_e for Shirasu soil.

Case No.	Water content in nature (%)	Void ratio ($p' = 10$ kPa)	Density of soil particle, (g/cm^3)	ρ_e (OCR)*
1	25.6	1.57	2.45	0.04 (1.5)
2	23.3	1.47	2.40	0.14 (4.0)
3	23.1	1.57	2.45	0.04 (1.5)

Note: *$\rho_e = \lambda - \kappa$ at overconsolidation; ** Data are from the work by Kitamura et al. (2007).

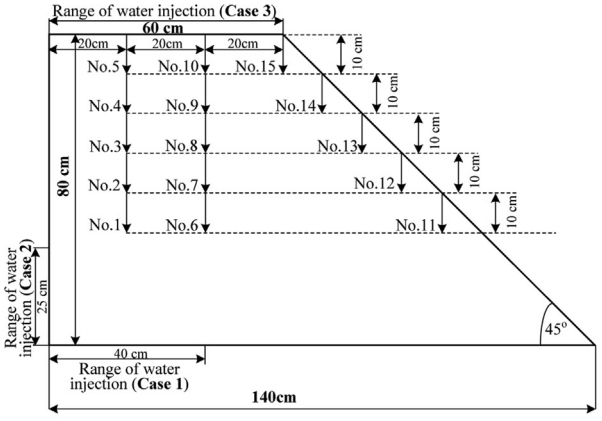

(a) Positions of measuring units and water injection.

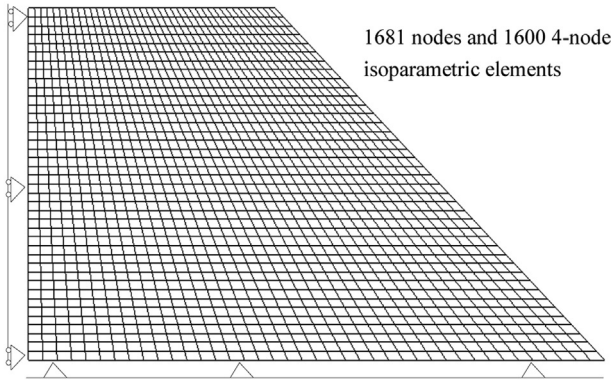

(b) FEM mesh.

Fig. 16. Layouts of measuring units, water injection positions and FEM mesh.

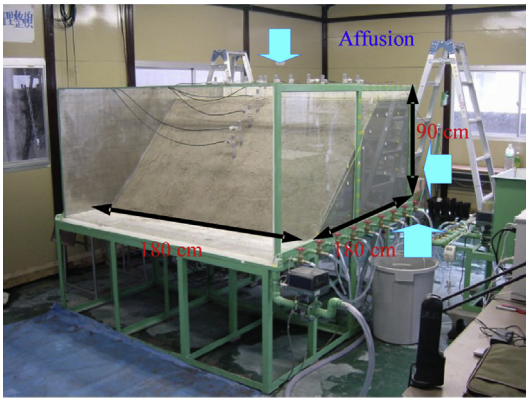

Fig. 15. Bird view of test apparatus and model ground (Kitamura et al., 2007).

Table 6
Material parameters of Shirasu soil.

Compression index, λ	Swelling index, κ	Critical state parameter, M	Void ratio N ($p' = 10$ kPa on N.C.L.)	Poisson's ratio, ν
0.105	0.007	0.47	1.59	0.30
Parameter of overconsolidation, a	Parameter of suction, b	Parameter of overconsolidation, β	Void ratio, N_r ($p' = 10$ kPa on N.C.L.S.)	
5.00	0.50	1.00	1.61	

Takeshita and Morii (2006) and Kamiya et al. (2006), the relation between the permeability and the degree of saturation used in the analysis is assumed as shown in Fig. 19.

In the numerical calculation, the first stage is to calculate the initial stress field by gravitational field; then a prescribed increment of water head is applied in the second stage. Fig. 20 shows the comparisons of the negative PWP between the test and the calculated results at some measured positions for 3 cases, respectively. From these figures, it is observed that the simulation can generally describe the development of PWP well on the whole in the points far away from the slope surface. In the points along the slope surface, however, a significant difference between the calculation and the test was observed. This might be caused by the assumption that the coefficients of permeability are the same in vertical and horizontal directions, and that the initial suction and the degree of saturation are the same in the whole model ground.

Fig. 21 shows the contours of the degree of saturation at different times in all three cases. In Case 1 and Case 2, it is known that the water is infiltrated gradually toward the slope surface from the initial position. In Case 1, the seepage of water is more intensive than that in Case 2. Therefore, 300 min after the start of the water infiltration, the soil at the toe of the slope is saturated earlier in Case 1 than in Case 2. In Case 3, the water is infiltrated from the top of the slope surface toward the bottom. It is known from the calculation that about 50 min after the seepage, the infiltrated water reached the bottom surface, and then the water began to accumulate at the left corner of the slope due to the impermeability of the bottom surface. An interesting phenomenon can be seen in Fig. 21c that until about 50 min, the degree of saturation at the top area is larger than that at the left bottom corner. After then, however, the situation became conversed, i.e. the degree of saturation at the left bottom corner is larger than that at the top area, showing clearly the migration process of the infiltrated water due to gravitational force.

Fig. 22 shows the change in the distribution of the plastic shear strain with elapsed time for all the three cases, where $\sqrt{2I_2^p}$ is the second invariant of deviatoric plastic strain tensor. It is found that the shear strain firstly occurred at the toe of slope in all cases, and then propagated backward toward the top surface. At the end of tests (also calculations), a shear band developed clearly in Case 1 and Case 3 but did not show up clearly in Case 2.

Fig. 23 shows the calculated displacement vectors at the end of tests (also calculations) in all cases. It is known from this figure that a larger displacement along the shear band toward the slope toe developed in Case 1 and Case 3. Compared the shear band formed in the slope shown in Fig. 16 with the stress paths shown in Fig. 17, it

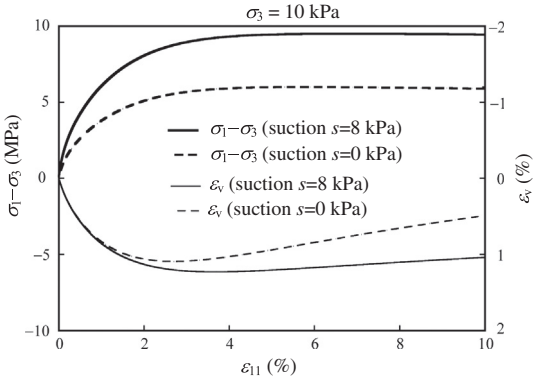

Fig. 17. Theoretical stress–strain-dilatancy relations of Shirasu soil under different constant suctions.

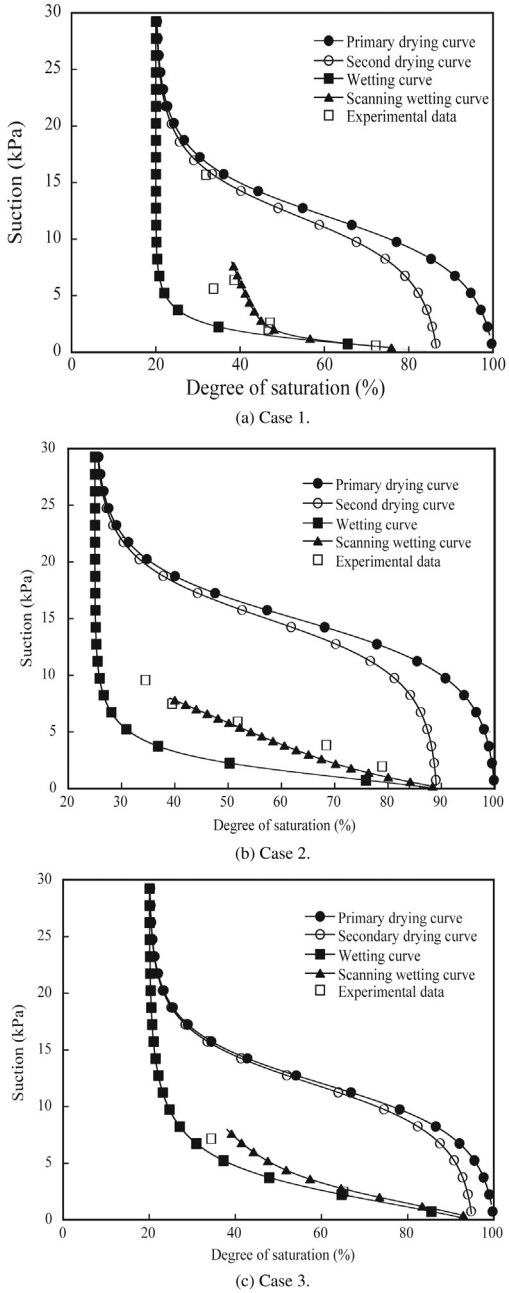

Fig. 18. MCC of Shirasu (test results by Kitamura et al., 2007).

Table 7
Parameters of MCC for Shirasu soil.

Case No.	Saturated degrees of saturation, S_r^s	Residual degrees of saturation, S_r^r	Parameter corresponding to drying AEV, S_d (kPa)	Parameter corresponding to wetting AEV, S_w (kPa)
1	0.87	0.20	12.0	0.07
2	0.89	0.25	15.0	0.10
3	0.95	0.20	12.0	0.17
Case No.	Initial stiffness of scanning curve, k_{sp}^e (kPa)	Parameter of shape function, c_1	Parameter of shape function, c_2	Parameter of shape function, c_3
1	90.0	0.30	0.60	30.0
2	20.0	0.30	0.40	50.0
3	50.0	0.33	0.18	5.0

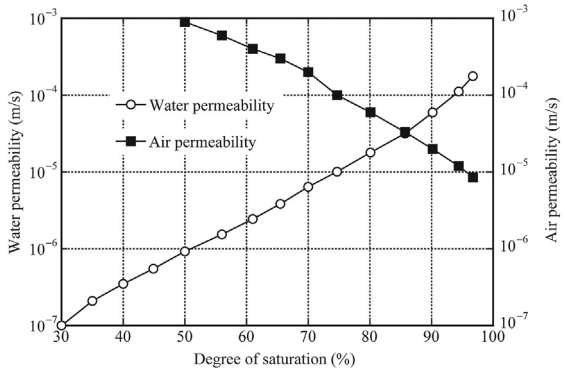

Fig. 19. Relations between water permeability and air with degree of saturation.

is reasonable to judge that the slope is more dangerous in Case 1 and Case 3 than in Case 2, which is consistent with the observed results in the tests that an entire slope failure had occurred in Case 1 and Case 3 (Kitamura et al., 2007). In Case 2, however, failure only happened in the area near the toe of the slope, where the maximum shear strain reached about 10%, as shown in Fig. 22.

Because the permeability of air for the Shirasu soils is very larger, the influence of the air pressure is very limited and can be neglected due to the vented condition in Case 1 and Case 2, where the air can be ventilated from the ground very easily due to the water injection from the bottom area. In Case 3, however, the permeability of air decreases significantly due to the infiltrated water at the top surface. As a result, the air pressure increased at the corner of the slope along with the seepage of water from the top

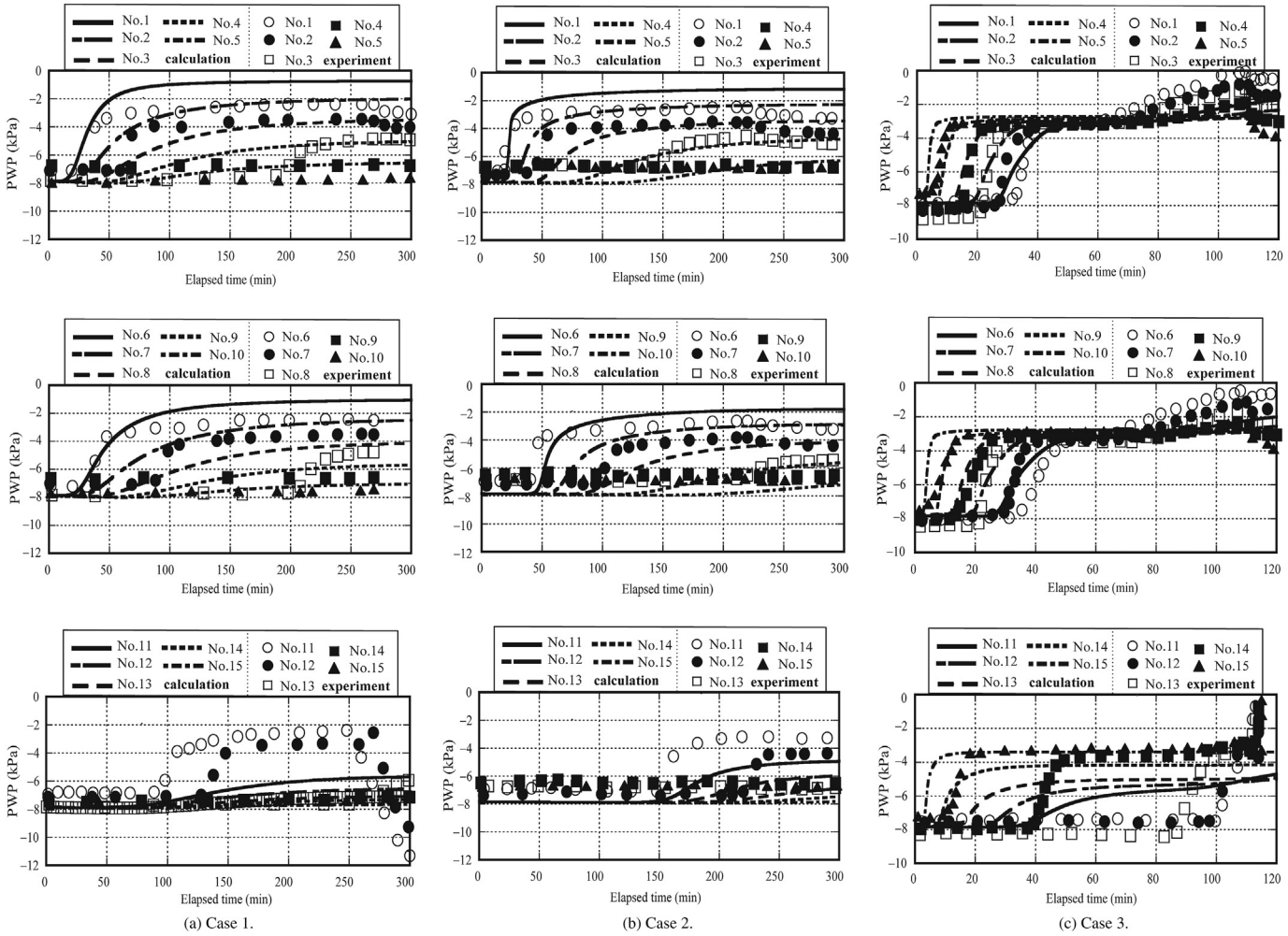

Fig. 20. Comparisons between test and calculated results of negative PWPs at some measured positions (test results by Kitamura et al., 2007).

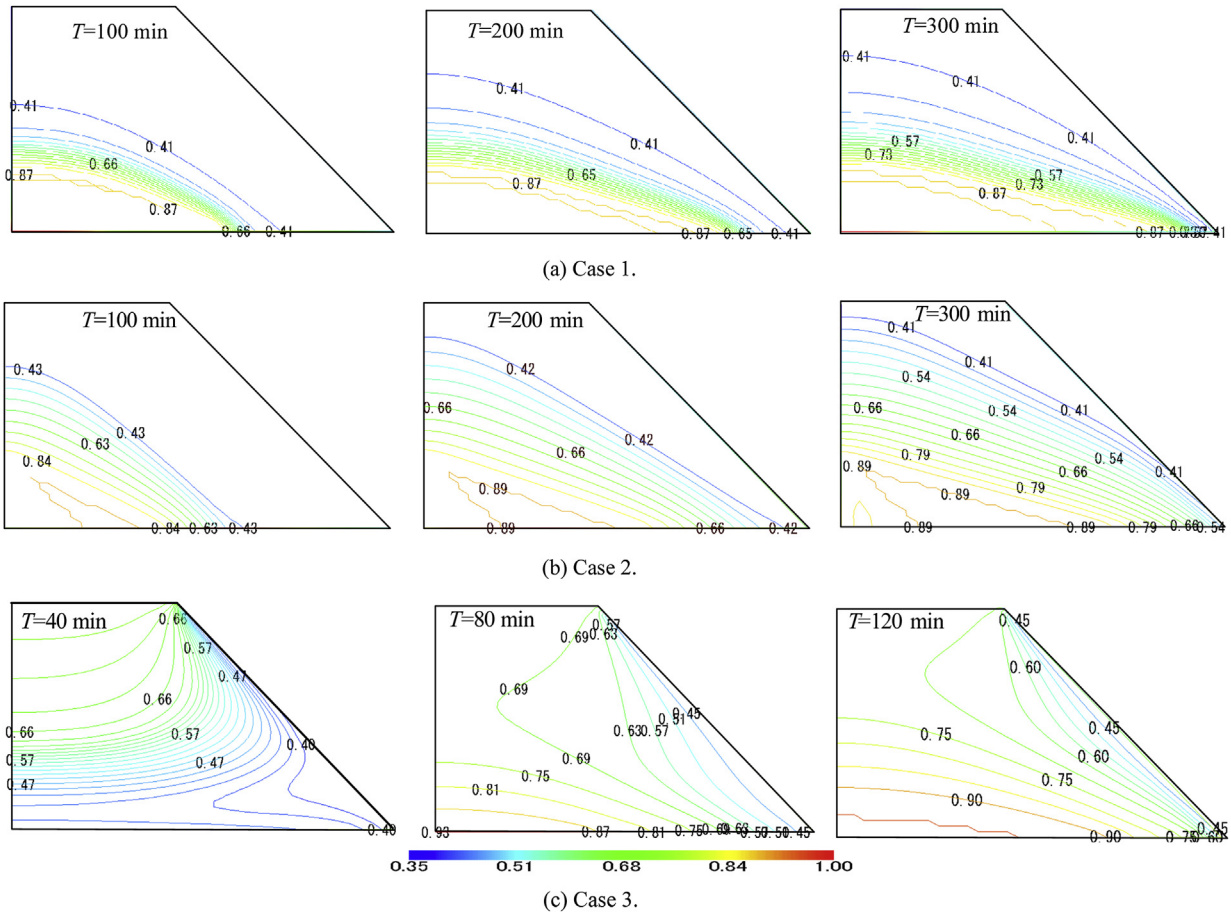

Fig. 21. Contours of the degrees of saturation at different times.

surface to the bottom surface, as shown in Fig. 24. When the infiltrated water reached the bottom surface, the air pressure reached its maximum value and then turned to decrease gradually due to the escape of the air from the vented boundaries at the top and slope surface. Though the value of PAP is very small compared with the PWP, the changing pattern with time is quite natural, because when the water infiltrates on the top of a river dike from rainfall, the vented boundary of the top surface will change to unvented one and the air within the area will be enclosed with the unvented boundaries and be compressed.

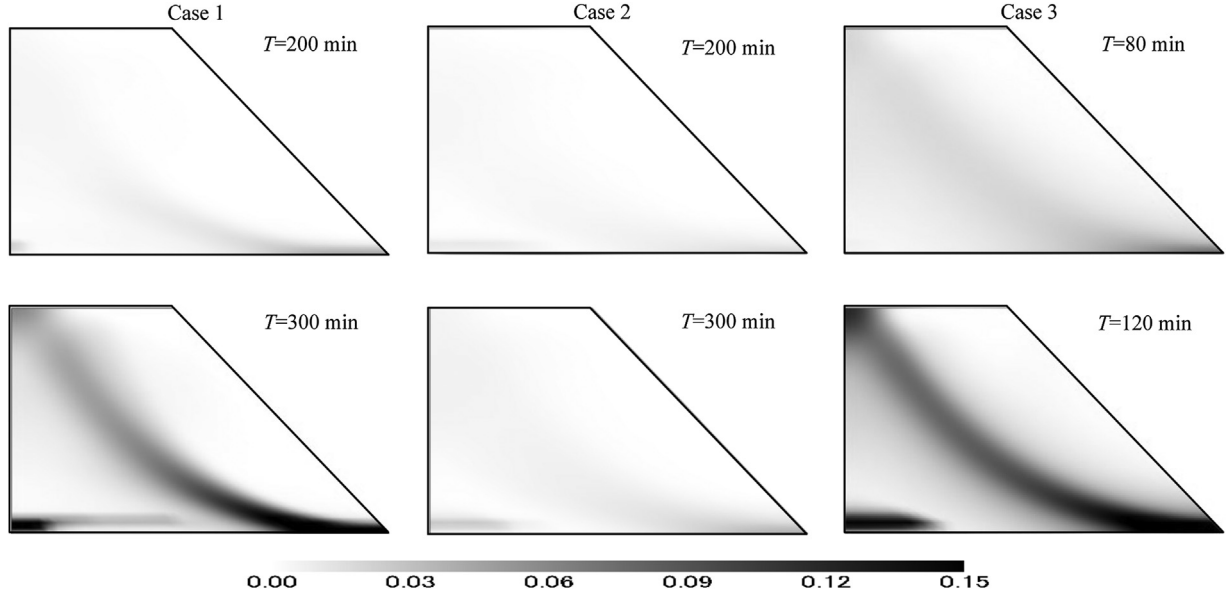

Fig. 22. Calculated distributions of plastic deviatoric strains ($\sqrt{2I_2^p}$) at different times.

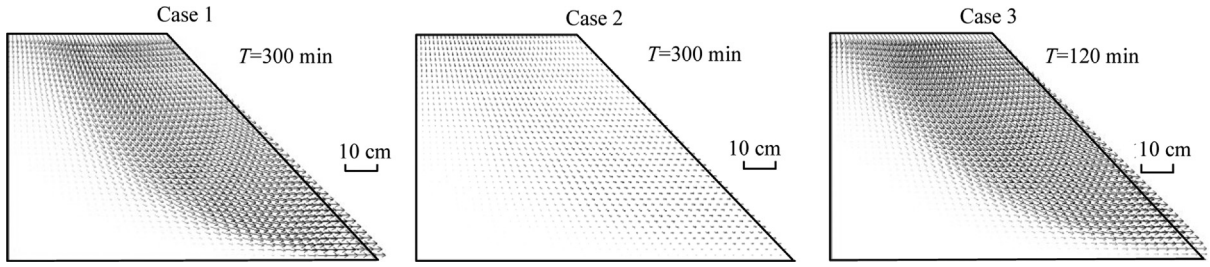

Fig. 23. Calculated displacement vectors at final stage.

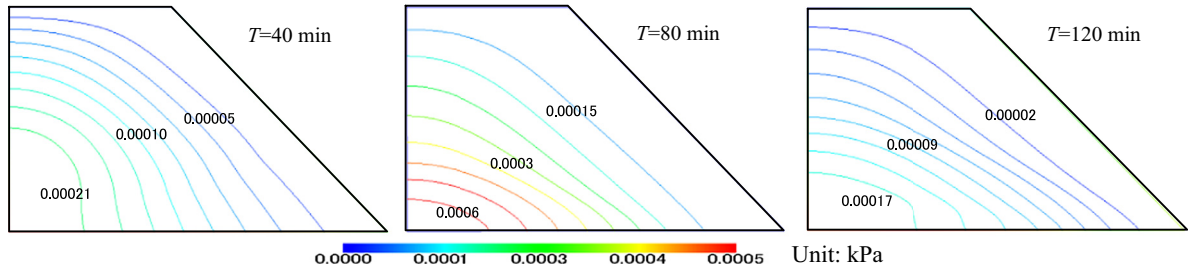

Fig. 24. Calculated distribution of air pressure at different times in Case 3 (unit: MPa).

5. Conclusions

In this paper, a FEM using unified field equations for the THMA coupling problem in finite deformation algorithm is derived based on the recently proposed thermo-elastoplastic constitutive model for unsaturated/saturated soil. In the field equations, the EPW, the PAP, the displacement of solid phase, and the temperature are used as the unknown variables. In discretizing the field equations of THMA coupling problem, FEM is used for spatial discretization of the equilibrium and the energy conservation equations, while the backward finite difference scheme is used for the spatial discretization of the continuity equations. The validity of the numerical method is verified by laboratory tests and in situ test. The following concluding remarks can be drawn:

(1) In the proposed numerical method, the THMA coupling problem in finite deformation algorithm is deduced with FEM using unified field equations. The constitutive model adopted in the field equations employs the Bishop-type skeleton stress, the degree of saturation and the temperature as its state variables, making it possible to describe the behavior of saturated/unsaturated soils under non-isothermal condition in a unified way.

(2) As a first verification of the proposed numerical method, an in situ heating test (Munoz, 2006) is simulated in order to investigate the THMA behavior of the bentonite-host rock composite structure under unsaturated condition. Based on the simulated results, it is known that the present simulation can properly describe the THMA behaviors observed in the heating test such as the hydration of water, the change of temperature, the evolution of EPWP on the whole. It is, therefore, reasonable to say that the proposed numerical method can be applied to investigate the real field problem in the deep geological repository of HLRW.

(3) The triaxial compression tests under undrained and unvented conditions were also simulated by the proposed method in order to verify its validity. In the simulation, the elementary behaviors of the triaxial tests are calculated with one-element 3D analysis. From the comparisons between the test and the simulation, it is found that the proposed numerical method can well describe the test behaviors such as the skeleton stress path, the stress–strain relation, and the developments of PWP and PAP at different suctions under isothermal condition.

(4) The model tests on slope failure due to water injection or rainfall have also been simulated by the same numerical method under isothermal condition. The behavior of the ground, such as the seepage of water due to rainfall or water injection, the change of the degree of saturation, the changes of PWP and PAP, the deformation of the model ground and the shear band formed in the slope failure, can be simulated on the whole in a unified way in comparison of the calculated results with the measured ones. It is particularly worth mentioning that due to the incorporation of a proper constitutive model for the saturated/unsaturated soil, the simulation can well describe the different failure patterns of the model ground observed in the tests. It is also interesting to note that all the material parameters of the Shirasu soils used in the analyses are the same for all the test cases, suggesting the application of the unified numerical method.

Conflict of interest

We wish to confirm that there are no known conflicts of interest associated with this publication and there has been no significant financial support for this work that could have influenced its outcome.

Appendix. Brief introduction of the constitutive model for unsaturated soils

In the proposed model, based on experimental results, a quantitative relation for void ratio-logarithmic mean skeleton stress (e-ln$p$) relation using the degree of saturation as a state variable is established. And it is assumed that normally consolidated line in unsaturated state (N.C.L.S.) is parallel to the normally consolidated line in saturated state (N.C.L.) but in a higher position than N.C.L., as shown in Fig. A1, which means that under the same mean skeleton stress, unsaturated soil can keep higher void ratio than those of saturated soil.

For N.C.L.S., we have:

$$e = N(S_r) - \lambda \ln \frac{p}{p_r} \quad \left(\eta = \frac{q}{p} = 0\right) \tag{A1}$$

For C.S.L.S., we have:

$$e = \Gamma(S_r) - \lambda \ln \frac{p}{p_r} \quad \left(\eta = \frac{q}{p} = M\right) \tag{A2}$$

where $N(S_r)$ and $\Gamma(S_r)$ are the void ratios at N.C.L.S. and C.S.L.S., respectively, under a reference mean skeleton stress p_r (usually $p_r = 98$ kPa) and certain degree of saturation; $p = \sigma_{ii}/3$ and $q = \sqrt{3(\sigma_{ij} - p\delta_{ij})(\sigma_{ij} - p\delta_{ij})/2}$ are the mean skeleton stress and the second invariant of deviatory skeleton stress tensor, respectively; M is the stress ratio at critical state and has the same value for saturated and unsaturated states. Therefore, similar to the derivation of Cam-Clay model for saturated soils, the void ratio e subjected to shearing is assumed to be:

$$e = \chi(\eta, S_r) - \lambda \ln \frac{p}{p_r} \tag{A3}$$

where $\chi(\eta, S_r)$ is a function of shear stress ratio η and the degree of saturation S_r and can be expressed with simple functions as:

(i) For Cam-Clay type (Roscoe et al., 1963):

$$e = N(S_r) - \frac{N(S_r) - \Gamma(S_r)}{M}\eta - \lambda \ln \frac{p}{p_r} \tag{A4}$$

(ii) For modified Cam-Clay type (Schofield and Wroth, 1968):

$$e = N(S_r) - \frac{N(S_r) - \Gamma(S_r)}{\ln 2} \ln \frac{M^2 + \eta^2}{M^2} - \lambda \ln \frac{p}{p_r} \tag{A5}$$

Under a saturated isotropic normally consolidated state, that is, $s = 0, p = p_0, \eta = 0, S_r = 1, N = N(S_r = 1)$, e takes a value of e_0 and can be expressed as

$$e_0 = N - \lambda \ln \frac{p_0}{p_r} \tag{A6}$$

The yield function for unsaturated soil using the skeleton stress and the degree of saturation as state variables can then be obtained as

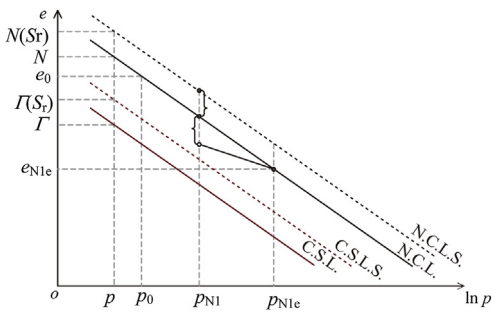

Fig. A1. Illustration of e-ln$p$ relation considering moving up of N.C.L. and C.S.L. due to insaturation.

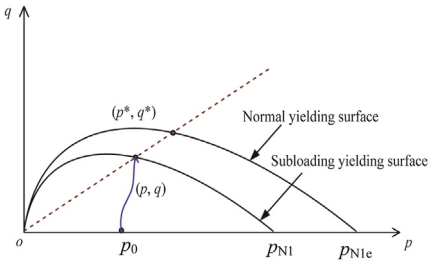

Fig. A2. Extension of sub-loading concept to unsaturated soil in skeleton stress space.

$$f = \ln \frac{p}{p_0} + \ln \frac{M^2 + \eta^2}{M^2} - \frac{\rho_s}{1 + e_0}\frac{1}{C_p} + \frac{\rho_e}{1 + e_0}\frac{1}{C_p} - \varepsilon_v^p \frac{1}{C_p} = 0 \tag{A7}$$

where

$$C_p = \frac{\lambda - \kappa}{1 + e_0},\ \rho_e = (\lambda - \kappa)\ln \frac{p_{N1e}}{p_{N1}},\ \rho_s = N(S_r) - N,$$
$$N = N(S_r = 1) \tag{A8}$$

where ρ_e represents a void ratio difference between the normally consolidated state and the overconsolidated state under the same mean skeleton stress. ρ_s represents a void ratio difference between N.C.L. and N.C.L.S. under the same mean skeleton stress. The yield surface is shown in Fig. A2. The model can take into consideration both the unsaturated condition and the overconsolidated state.

As to the thermal effect, the concept of the equivalent stress proposed by Zhang and Zhang (2009) is adopted:

$$\tilde{p}_N = p_N + 3K^s \alpha_T^s (\theta - \theta_0) \tag{A9}$$

where p_N is the current mean stress; K^s is the bulk modulus of solid phase of soil; θ is the present temperature; θ_0, a reference temperature, is an arbitrary value and is taken as the global average temperature, i.e. 15 °C; α_T^s is the linear thermal expansion coefficient of solid phase of soil whose value should be negative because compression is usually taken as positive in geomechanics.

It is known that the pre-consolidation stress decreases with the increase of the temperature from the experimental results discussed in the previous section, in other words, the over-consolidation rate (OCR) decreases with the increase of temperature. Therefore, the equivalent void ratio difference $\tilde{\rho}_e$ considering the influence of temperature is given as

$$\tilde{\rho}_e = (\lambda - \kappa)\ln[(\tilde{p}_{N1} OCR)/p_{N1}] \tag{A10}$$

where $\tilde{p}_{N1}$ is the initial equivalent mean stress, and p_{N1} is the initial mean stress.

Therefore, the yielding function Eq. (A7) can be written in the equivalent mean stress space as

$$f = \ln \frac{p}{p_0} + \ln \frac{M^2 + \eta^2}{M^2} - \frac{\rho_s}{1 + e_0}\frac{1}{C_p} + \frac{\tilde{\rho}_e}{1 + e_0}\frac{1}{C_p} - \varepsilon_v^p \frac{1}{C_p} = 0 \tag{A11}$$

From consistency equation $df = 0$, it is known that

$$df = \frac{\partial f_\sigma}{\partial \sigma_{ij}} d\sigma_{ij} - d\left(\frac{\rho_s}{1 + e_0}\right)\frac{1}{C_p} + d\left(\frac{\tilde{\rho}_e}{1 + e_0}\right)\frac{1}{C_p} - d\varepsilon_v^p \frac{1}{C_p} = 0 \tag{A12}$$

where

$$f_\sigma = \ln \frac{p}{p_0} + \ln \frac{M^2 + \eta^2}{M^2} \tag{A13}$$

In Eq. (A12), it is necessary to give evolution equations for the development of the state variables $\tilde{\rho}_e$ of OCR and ρ_s of saturation, and the flow rule for plastic strain tensor in the following ways:

(i) Step 1

Associated flow rule:

$$d\varepsilon_{ij}^{p} = \Lambda \frac{\partial f}{\partial \sigma_{ij}} \tag{A14}$$

(ii) Step 2

$$d\left(\frac{\tilde{\rho}_e}{1+e_0}\right) = -\Lambda \frac{\rho^{\beta}}{\tilde{p}},\ \rho = a\tilde{\rho}_e + b\rho_s \tag{A15}$$

(iii) Step 3

$$\left.\begin{aligned} N\left(S_r\right) &= N + \frac{N_r - N}{S_r^s - S_r^r}\left(S_r^s - S_r\right);\ N_r = N\left(S_r^r\right) \\ \rho_s &= N\left(S_r\right) - N = Q\left(S_r^s - S_r\right);\ Q = \frac{N_r - N}{S_r^s - S_r^r} \\ d\rho_s &= -Q dS_r \end{aligned}\right\} \tag{A16}$$

where S_r^r and S_r^s are the degrees of saturation under residual and saturated conditions. Eq. (A16) means that $N(S_r)$ changes linearly with the degree of saturation. Parameters a, b and β control the development of the state variables $\tilde{\rho}_e$, and N_r is the void ratios at N.C.L.S. under the reference mean skeleton stress p_r when the degrees of saturation are in residual state, that is, $N_r = N(S_r^r)$.

Volumetric strain increment can be divided into elastic and plastic parts as

$$d\varepsilon_{ij} = d\varepsilon_{ij}^{e} + d\varepsilon_{ij}^{p} \tag{A17}$$

Using Hooke's theory with stiffness tensor E_{ijkl}, the incremental stress tensor can be expressed as

$$d\sigma_{ij} = E_{ijkl}\left(d\varepsilon_{kl} - d\varepsilon_{kl}^{p} - d\varepsilon_{kl}^{T}\right) = E_{ijkl}d\varepsilon_{kl} - E_{ijkl}\Lambda\frac{\partial f}{\partial \sigma_{kl}} - E_{ijkl}d\varepsilon_{kl}^{T} \tag{A18}$$

Substituting this equation into Eq. (A12), the following relation can be obtained:

$$\frac{\partial f}{\partial \sigma_{ij}}E_{ijkl}d\varepsilon_{kl} - \frac{\partial f}{\partial \sigma_{ij}}E_{ijkl}\Lambda\frac{\partial f}{\partial \sigma_{kl}} - \frac{\partial f}{\partial \sigma_{ij}}E_{ijkl}d\varepsilon_{kl}^{T} - \Lambda\frac{\rho^{\beta}}{\tilde{p}}\frac{1}{C_p} + \frac{Q}{1+e_0}dS_r\frac{1}{C_p} - \Lambda\frac{1}{C_p}\frac{\partial f}{\partial \sigma_{mm}} = 0 \tag{A19}$$

which results in:

$$\Lambda = \frac{\frac{\partial f}{\partial \sigma_{ij}}E_{ijkl}d\varepsilon_{kl} + \frac{1}{C_p}\frac{Q}{1+e_0}dS_r - \frac{\partial f}{\partial \sigma_{ij}}E_{ijkl}d\varepsilon_{kl}^{T}}{\frac{h_p}{C_p} + \frac{\partial f}{\partial \sigma_{ij}}E_{ijkl}\frac{\partial f}{\partial \sigma_{kl}}} \tag{A20}$$

where

$$h_p = \frac{\partial f}{\partial \sigma_{mm}} + \frac{\rho^{\beta}}{\tilde{p}} \tag{A21}$$

Therefore it is easy to define the loading criteria as

$$\left.\begin{aligned} &\Lambda > 0 \quad loading \\ &\Lambda = 0 \quad neutral \\ &\Lambda < 0 \quad unloading \end{aligned}\right\} \tag{A22}$$

Substituting Eq. (A20) into Eq. (A14), we have

$$d\varepsilon_{ij}^{p} = \frac{\frac{\partial f}{\partial \sigma_{mn}}E_{mnkl}d\varepsilon_{kl} + \frac{1}{C_p}\frac{Q}{1+e_0}dS_r - \frac{\partial f}{\partial \sigma_{mn}}E_{mnkl}d\varepsilon_{kl}^{T}}{\frac{h_p}{C_p} + \frac{\partial f}{\partial \sigma_{mn}}E_{mnkl}\frac{\partial f}{\partial \sigma_{kl}}}\frac{\partial f}{\partial \sigma_{ij}} \tag{A23}$$

Meanwhile,

$$\begin{aligned} d\sigma_{ij} =& E_{ijkl}\left(d\varepsilon_{kl} - d\varepsilon_{kl}^{p} - d\varepsilon_{kl}^{T}\right) = E_{ijkl}d\varepsilon_{kl} - E_{ijkl}\Lambda\frac{\partial f}{\partial \sigma_{kl}} \\ &- E_{ijkl}d\varepsilon_{kl}^{T} = E_{ijkl}d\varepsilon_{kl} - E_{ijqr}E_{mnkl}\frac{\partial f}{\partial \sigma_{mn}}\frac{\partial f}{\partial \sigma_{qr}}\frac{1}{\tilde{D}}d\varepsilon_{kl} \\ &- \frac{1}{C_p}\frac{Q}{1+e_0}dS_r\frac{1}{\tilde{D}}E_{ijqr}\frac{\partial f}{\partial \sigma_{qr}} + \frac{1}{\tilde{D}}\frac{\partial f}{\partial \sigma_{mn}}\frac{\partial f}{\partial \sigma_{qr}}E_{ijqr}E_{mnkl}d\varepsilon_{kl}^{T} \\ &- E_{ijkl}d\varepsilon_{kl}^{T} = \left(E_{ijkl} - E_{ijkl}^{p}\right)d\varepsilon_{kl} - E_{ij}^{RFS}dS_r \\ &- \left(E_{ijkl} - E_{ijkl}^{p}\right)d\varepsilon_{kl}^{T} = E_{ijkl}^{ep}d\varepsilon_{kl} - E_{ij}^{RFS}dS_r - E_{ijkl}^{ep}d\varepsilon_{kl}^{T} \end{aligned} \tag{A24}$$

where

$$\tilde{D} = \frac{h_p}{C_p} + \frac{\partial f}{\partial \sigma_{mn}}E_{mnkl}\frac{\partial f}{\partial \sigma_{kl}} \tag{A25}$$

$$E_{ijkl}^{p} = \frac{E_{ijqr}E_{mnkl}\frac{\partial f}{\partial \sigma_{mn}}\frac{\partial f}{\partial \sigma_{qr}}}{\tilde{D}} \tag{A26}$$

$$E_{ijkl}^{ep} = E_{ijkl} - E_{ijkl}^{p} \tag{A27}$$

$$E_{ij}^{RFS} = \frac{1}{C_p}\frac{Q}{1+e_0}\frac{1}{\tilde{D}}E_{ijkl}\frac{\partial f}{\partial \sigma_{kl}} \tag{A28}$$

References

Akai K, Tamura T. Numerical analysis of multi-dimensional consolidation accompanied with elasto-plastic constitutive equation. Journal of Japanese Civil Engineering Society 1978;269:95–104 (in Japanese).

Akesson M, Jacinto AC, Gatabin C, Sanchez M, Ledesma A. Bentonite THM behavior at high temperatures: experimental and numerical analysis. Geotechnique 2009;59(4):307–18.

Alonso EE, Gens A, Josa A. A constitutive model for partially saturated soils. Geotechnique 1990;40(3):405–30.

Baldi G, Hueckel T, Pellegrini R. Thermal volume changes of the mineral-water system in low porosity clay soils. Canadian Geotechnical Journal 1988;25(4):807–25.

Baldi G, Hueckel T, Peano A, Pellegrini R. Developments in modelling of thermo-hydro-geomechanical behaviour of boom clay and clay-based buffer materials. Commission of the European Communities: Report 13365/2 EN; 1991.

Borja RI. Conservation laws for three-phase partially saturated granular media. Unsaturated Soils: Numerical and Theoretical Approaches 2005;94:3–14.
Campanella RG, Mitchell JK. Influence of temperature variations on soil behavior. Journal of Soil Mechanics & Foundations Division, ASCE 1968;94(3):709–34.
Cekerevac C, Laloui L. Experimental study of thermal effects on the mechanical behavior of a clay. International Journal for Numerical and Analytical Method in Geomechanics 2004;28(3):209–28.
Chiu CF, Ng CWW. A state-dependent elasto-plastic model for saturated and unsaturated soils. Geotechnique 2003;53(9):809–29.
Cui YJ, Delage P. Yielding and plastic behaviour of an unsaturated compacted silt. Geotechnique 1996;46(2):291–311.
Cui YJ, Sultan N, Delage P. A thermomechanical model for saturated clays. Canadian Geotechnical Journal 2000;37(3):607–20.
Cui YJ, Le TT, Tang AM, Delage P, Li XL. Investigating the time-dependent behavior of Boom clay under thermomechanical loading. Geotechnique 2009;59(4):319–29.
Dumont M, Taibi S, Fleureau JM, Abou-Bekr N, Saouab A. A thermo-hydro-mechanical model for unsaturated soils based on the effective stress concept. International Journal of Numerical and Analytical Method in Geomechanics 2011;35(12):1299–317.
Francois B, Laloui L. ACMES-TS: constitutive model for unsaturated soils under non-isothermal conditions. International Journal of Numerical and Analytical Method in Geomechanics 2008;32:1955–88.
Gens A, Vaunat J, Garitte B, Wileveau Y. In situ behavior of a stiff layered clay subject to thermal loading: observations and interpretation. Geotechnique 2007;57(2):207–28.
Gens A, Sanchez M, Do L, Guimaraes N, Alonso EE, Lloret A, Olivella S, Villar MV, Huertas F. A full-scale in situ heating test for high-level nuclear waste disposal: observations, analysis and interpretation. Geotechnique 2009;59(4):377–99.
Gens A. Soil-environment interactions in geotechnical engineering. Geotechnique 2010;60(1):3–74.
Jia Y, Wileveau Y, Su K, Duveau G, Shao JF. Thermo-hydro-mechanical modeling of a situ heating experiment. Geotechnique 2007;57(10):845–55.
Kamiya K, Bakrie R, Honjo Y. The measurement of air permeability coefficient of unsaturated soil with controlling water retentivity. Proceedings of JSCE 2006;62(3):679–88 (in Japanese).
Kitamura R, Haruyama M, Misumi K. Mechanical properties of Shirasu under intermediate and low pressures. Japanese Geotechnical Journal 1984;32(2):17–21 (in Japanese).
Kitamura R, Sako K, Kato S, Mizushima T, Imanishi H. Soil tank test on seepage and failure behaviors of Shirasu slope during rainfall. Japanese Geotechnical Journal 2007;2(3):149–68 (in Japanese).
Kohgo Y, Nakano M, Miyazaki T. Theoretical aspects of constitutive modelling for unsaturated soils. Soils and Foundations 1993;33(4):49–63.
Laloui L. Thermo-mechanical behaviour of soils. Environmental Geomechanics 2001;5(6):809–43.
Laloui L, Cekerevac C. Thermo-plasticity of clays: an isotropic yield mechanism. Computers and Geotechnics 2003;38(8):649–60.
Li C, Borja RI, Regueiro RA. Dynamics of porous media at finite strain. Computer Methods in Applied Mechanics and Engineering 2004;193(36–38):3837–70.
Loret B, Khalili N. An effective stress elastic-plastic model for unsaturated porous media. Mechanics of Materials 2002;34(2):97–116.
Munoz J. Thermo-hydro-mechanical analysis of soft rock, application to a large scale heating test and large scale ventilation test. PhD Thesis. Catalonia, Spain: Polytechnic University of Catalonia; 2006.
Nguyen TS. Computational modeling of thermal-hydrological-mechanical processes in geological media. PhD Thesis. Montreal, Quebec, Canada: McGill University; 1995.
Nishimura T. Experimental research and modeling of thermo-creep behavior of sedimentary soft rock and its application to BVP. MS Thesis. Nagoya: Nagoya Institute of Technology; 2013.
Ohno S, Kawai K, Tachibana S. Elasto-plastic constitutive model for unsaturated soil applied effective degree of saturation as parameter expressing stiffness. Journal of Japanese Civil Engineering Society 2007;63(4):1132–41 (in Japanese).
Oka F, Yashima A, Shibata T, Shibata T, Kato M, Uzuoka R. FEM-FDM coupled liquefaction analysis of a porous soils using an elasto-plastic model. Applied Scientific Research 1994;52(3):209–45.
Oka F, Kimoto S, Takada N, Gotoh H, Higo Y. A seepage-deformation coupled analysis of an unsaturated river embankment using a multiphase elasto-viscoplastic theory. Soil and Foundations 2010;50(4):483–94.
Okada T. Mechanical properties of sedimentary soft rock at high temperatures (Part 1)—Evaluation of temperature dependency based on triaxial compression test. Tokyo: Civil Engineering Research Laboratory Report, No. N04026; 2005 (in Japanese).
Okada T. Mechanical properties of sedimentary soft rock at high temperatures (Part 2)—Evaluation of temperature dependency of creep behavior based on unconfined compression test. Tokyo: Civil Engineering Research Laboratory Report, No. N05057; 2006 (in Japanese).
Roscoe KH, Schofield AN, Thurairajah A. Yielding of clay in states wetter than critical. Geotechnique 1963;13(3):211–40.
Sawada M, Okada T, Tani K, Takakura N, Ikenoya T. In-situ heating test in the sedimentary soft rock (Part 2)—Application of thermo-hydro-mechanical coupled analysis to the sedimentary soft rock. Tokyo: Civil Engineering Research Laboratory Report, No. N08055; 2009 (in Japanese).
Schofield AN, Wroth CP. Critical state soil mechanics. London: McGraw-Hill; 1968.
Sheng D, Fredlund DG, Gens A. A new modelling approach for unsaturated soils using independent stress variables. Canadian Geotechnical Journal 2008;45(4):511–34.
Sun DA, Cui HB, Matsuoka H, Sheng D. A three-dimensional elastoplastic model for unsaturated compacted soils with hydraulic hysteresis. Soils and Foundations 2007;47(2):253–64.
Takeshita Y, Morii T. Field measurement of field saturated and unsaturated hydraulic conductivity using soil moisture profile. Journal of Japanese Civil Engineering Society 2006;62(4):831–9 (in Japanese).
Towhata I, Kuntiwattanaku P, Seko I, Ohishi K. Volume change of clays induced by heating as observed in consolidation tests. Soils and Foundations 1993;33(4):170–83.
Uchaipichat A, Khalili N. Experimental investigation of thermo-hydro-mechanical behaviour of an unsaturated silt. Geotechnique 2009;59(4):339–53.
Uzuoka R. Effective stress analysis (finite deformation scheme). Private discussion; 2010 (in Japanese).
Uzuoka R, Kamura A, Sento N, Kazama M. Finite element analysis for dynamic finite deformation in unsaturated soil. Proceedings of the Conference on Computational Engineering and Science 2007;12(2):523–6 (in Japanese).
Uzuoka R, Kurihara T, Kazama M, Sento N. Finite element analysis of coupled of unsaturated soil and water using aerial elements. Proceedings of the Conference on Computational Engineering and Science 2008;13(1):219–22 (in Japanese).
Uzuoka R, Kamiya K, Chiba T, Mori T, Kazama M. Soil–water–air coupled dynamic analysis of unsaturated fill. Proceedings of the Conference on Computational Engineering and Science 2009;14(1):461–4 (in Japanese).
Xiong YL. Thermo-hydraulic-mechanical-air coupling finite element analysis and its application to geotechnical engineering problems. PhD Thesis. Nagoya, Japan: Nagoya Institute of Technology; 2013. pp. 37–76.
Yatomi C, Yashima A, Iizuka A, Sano I. General theory of shear bands formation by a non-coaxial Cam-Clay model. Soils and Foundations 1989;29(3):41–53.
Zhang F, Ikariya T. A new model for unsaturated soil using skeleton and degree of saturation as state variables. Soil and Foundations 2011;51(1):67–81.
Zhang S, Zhang F. A thermo-elasto-viscoplastic model for soft sedimentary rock. Soils and Foundations 2009;49(4):583–95.
Zhang S, Leng WM, Zhang F, Xiong YL. A simple thermo-elastoplastic model for geomaterials. International Journal of Plasticity 2012;34:93–113.
Zhou AN, Sheng DC, Sloan SW, Gens A. Interpretation of unsaturated soil behaviour in the stress-saturation space, I: volumetric change and water retention behaviour. Computers and Geotechnics 2012a;43:178–87.
Zhou AN, Sheng DC, Sloan SW, Gens A. Interpretation of unsaturated soil behaviour in the stress-saturation space, II: constitutive relationships and validations. Computers and Geotechnics 2012b;43:111–23.

Dr. Feng Zhang, born in 1959, is now Professor of Department of Civil Engineering, Nagoya Institute of Technology, Japan. He got Bachelor of Science in Mathematics & Mechanics, Nanjing University of Science & Technology, Nanjing, China in 1982; and Master of Science in Engineering Mechanics, Tongji University, China in 1989. He got Ph.D. in Civil Engineering, Kyoto University, Japan in 1995. His research interests cover soil mechanics & rock mechanics, constitutive modeling of geomaterials, numerical analyses in geotechnical engineering, and seismic evaluation of earth structures.